HHS Public Access

Author manuscript

Nat Immunol. Author manuscript; available in PMC 2023 April 07.

Published in final edited form as:

Nat Immunol. 2021 January ; 22(1): 53–66. doi:10.1038/s41590-020-00818-9.

MEK inhibition reprograms CD8+ T lymphocytes into memory stem cells with potent antitumor effects

Vivek Verma[1,2], **Nazli Jafarzadeh**[1], **Shannon Boi**[3], **Subhadip Kundu**[1], **Zhinuo Jiang**[1], **Yiping Fan**[4], **Jose Lopez**[1], **Rahul Nandre**[1,7], **Peng Zeng**[2,8], **Fatmah Alolaqi**[1], **Shamim Ahmad**[2,9], **Pankaj Gaur**[1], **Simon T. Barry**[5], **Viia E. Valge-Archer**[5], **Paul D. Smith**[5], **Jacques Banchereau**[6], **Mikayel Mkrtichyan**[1], **Benjamin Youngblood**[3], **Paulo C. Rodriguez**[2,10], **Seema Gupta**[1,2], **Samir N. Khleif**[1,2,✉]

[1]The Loop Immuno-Oncology Laboratory, Lombardi Comprehensive Cancer Center, Georgetown University Medical Center, Washington, DC, USA.

[2]Georgia Cancer Center, Augusta University, Augusta, GA, USA.

[3]Department of Immunology, St. Jude Children's Research Hospital, Memphis, TN, USA.

[4]Center for Applied Bioinformatics, St. Jude Children's Research Hospital, Memphis, TN, USA.

[5]Bioscience, Early Oncology, AstraZeneca, Cambridge, UK.

[6]The Jackson Laboratory for Genomic Medicine, Farmington, CT, USA.

[7]Present address: Division of Preclinical Innovation, National Center for Advancing Translational Sciences, NIH, Rockville, MD, USA.

✉**Correspondence and requests for materials** should be addressed to S.N.K. snk48@georgetown.edu.

Author contributions

V.V., S.G. and S.N.K. conceived the study and designed the experiments. V.V. performed the experiments with input from N.J., S.K., Z.J., J.L., R.N., P.Z., F.A., S.A., P.G. and M.M. S.T.B., V.E.V.-A. and P.D.S. supplied the materials. B.Y. and S.B. performed the methylation experiment. Y.F. analyzed the whole-genome bisulfite sequencing. J.B. helped with the electron microscopy and, along with B.Y. and S.B., was involved in numerous discussions and reviewed the manuscript. P.C.R. helped with the metabolic assays. V.V., S.G. and S.N.K. analyzed the data and wrote the manuscript. S.N.K. supervised the study.

Online content

Any methods, additional references, Nature Research reporting summaries, source data, extended data, supplementary information, acknowledgements, peer review information; details of author contributions and competing interests; and statements of data and code availability are available at https://doi.org/10.1038/s41590-020-00818-9.

Competing interests

S.N.K. and V.V. are inventors on patent applications related to work on the induction of T_{SCM} by MEK1/2 inhibition in T cells and methods for use of these T_{SCM} in various therapeutic applications. S.N.K. reports honoraria from Syndax, IOBiotech, Bioline Therapeutics, Northwest Biotherapeutics, Advaxis, EMD Serono, GSK, UbiVac, McKinsey, AstraZeneca and Lycera. S.N.K. reports stocks or ownership interest in Advaxis, GeorgiaImmune, IOBiotech and Northwest Therapeutics. S.N.K. is a consultant for Syndax, IOBiotech, Bioline, Kahr, PDS Biotechnology, AstraZeneca, CytomX, NewLink Genetics, AratingaBio, CanImGuide and Lycera. S.N.K. is a board member for Advaxis. S.N.K. has research contracts with Syndax, IOBiotech, Bioline Therapeutics, AstraZeneca, MedImmune and Lycera. J.B. is on the Board of Directors of Neovacs and Stamford Pharmaceutical and is a member of the CUE Biopharma and GeorgiaImmune SABs. J.B. reports stock or ownership interest in Neovacs, Stamford Pharmaceuticals and Cue Biopharma. J.B. has a research contract with Sanofi.

Additional information

Extended data is available for this paper at https://doi.org/10.1038/s41590-020-00818-9.

Supplementary information is available for this paper at https://doi.org/10.1038/s41590-020-00818-9.

Peer review information Zoltan Fehervari was the primary editor on this article and managed its editorial process and peer review in collaboration with the rest of the editorial team.

[8]Present address: Department of Pharmacology, Case Western Reserve University, Cleveland, OH, USA.

[9]Present address: Kite Pharma/A GILEAD Company, Emeryville, CA, USA.

[10]Present address: H. Lee Moffitt Cancer Center & Research Institute, Tampa, FL, USA.

Abstract

Regenerative stem cell–like memory (T_{SCM}) $CD8^+$ T cells persist longer and produce stronger effector functions. We found that MEK1/2 inhibition (MEKi) induces T_{SCM} that have naive phenotype with self-renewability, enhanced multipotency and proliferative capacity. This is achieved by delaying cell division and enhancing mitochondrial biogenesis and fatty acid oxidation, without affecting T cell receptor-mediated activation. DNA methylation profiling revealed that MEKi-induced T_{SCM} cells exhibited plasticity and loci-specific profiles similar to bona fide T_{SCM} isolated from healthy donors, with intermediate characteristics compared to naive and central memory T cells. Ex vivo, antigenic rechallenge of MEKi-treated $CD8^+$ T cells showed stronger recall responses. This strategy generated T cells with higher efficacy for adoptive cell therapy. Moreover, MEKi treatment of tumor-bearing mice also showed strong immune-mediated antitumor effects. In conclusion, we show that MEKi leads to $CD8^+$ T cell reprogramming into T_{SCM} that acts as a reservoir for effector T cells with potent therapeutic characteristics.

Exhaustion of effector T cells, which results in their short persistence, is an important factor that limits the efficacy of immunotherapy[1]. Therefore, development of agents that can overcome these limitations is urgently needed. Targeted therapies with small-molecule inhibitors (SMIs) have been used successfully as anticancer agents[2,3]. Some of these molecules may provide tools that can modulate immune responses. Therefore, an understanding of the mechanisms of action of these inhibitors, particularly their immune modulatory effects, would help to better harness their antitumor potential, either alone or in combination with other therapies.

The mitogen-activated protein kinase (MAPK) pathway relays external mitogenic cues to the immune cells, leading to modulation of cellular differentiation and metabolic machinery that prepares the cells for effector functions[4,5]. In recent years, the mechanistic link between the metabolism of T cells and their effector functions, and the development of exhaustion, have emerged as important therapeutic targets for patients with cancer[6]. In the tumor microenvironment (TME), persistent mitogenic stimulation induces excessive division of effector cells, generating an exhausted phenotype that shows diminished effector functions and also compromises the generation of immune memory[7]. Inhibition of MEK (MEKi) potentiates the antitumor effects of immunotherapy with checkpoint inhibitors, as well as adoptive T cell transfer therapy (ACT)[8–10]. These effects of MEKi are mediated, in part, by increasing tumor immunogenicity[11] and modulation of the TME[9,10,12]. However, the effects of MEKi on T cell functionality, and their differentiation and memory generation, are poorly understood. Despite compromised cellular priming in the tumor-draining lymph nodes, MEKi treatment led to increased accumulation of activated $CD8^+$ T cells in the TME[9]. Therefore, an understanding of the immune modulatory mechanisms is essential to develop new and effective therapeutic strategies utilizing MEKi. Accordingly, here we

investigated the role of MEK inhibition in $CD8^+$ T cell metabolic reprogramming and in cell cycle progression and, in turn, its immunomodulatory effects on the TME.

We demonstrate that inhibition of the MAPK pathway by MEK1/2i induces strong antitumor activity through metabolic reprogramming of effector $CD8^+$ T cells. MEK1/2i during initial antigen priming suppresses cyclin D1, delaying cell cycle progression and enhancing metabolic fitness by modulating the ERK1/2–cyclin D1–PGC1α (peroxisome proliferator-activated receptor gamma coactivator 1 alpha)–SIRT3–FAO (fatty acid oxidation) pathway, which facilitates the generation of stem cell–like memory (T_{SCM}) cells[13]. These T_{SCM} cells are distinct from central memory (T_{CM}) cells in having higher self-renewability, multipotency and proliferation capacity, and higher methylation of effector genes, and from T_{naive} cells in having lower methylation of effector genes and open loci at *Tcf7* (ref. [14]). These MEKi-induced T_{SCM} showed strong cellular activation, high antigen-specific recall responses and prolonged survival. Accordingly, MEKi leads to the generation of $CD8^+$ effector T cells that are highly active and less exhausted, demonstrating potent antitumor activity in vivo and after ACT.

Results

MEKi enhances antitumor effects by preventing exhaustion and facilitating activation of effector $CD8^+$ T cells in the TME.

Molecular-targeted therapy using MEKi improves the antitumor effect of immunotherapy[10]. However, the mechanisms by which MEKi affects the immune response are not well understood. We tested the immune effects of selumetinib (AZD6244, ARRY-142886), a MEK1/2 inhibitor[15], in mouse tumor models that carry specific antigens, TC-1 (HPV16E7) and B16F10 (gp100). Vaccination (Vax) with the specific antigen generates a measurable effector immune response, which helps in dissecting the effect of MEKi on specific antitumor immunity. MEKi significantly enhanced the vaccine-specific antitumor response in both models (Fig. 1a,b). In the TC-1 tumor model, 50% of the mice survived in the MEKi plus Vax group, while only 10% survived in the Vax-treated group at day 40 (Fig. 1a, rightmost panel). The survival for these groups was 40% and 0%, respectively, in the B16F10 tumor model at day 28 (Fig. 1b, rightmost panel).

The chronic antigenic stimulation in the immunosuppressive TME induces a tonic MAPK signaling that renders the effector cells exhausted[7]. Since we observed robust antitumor responses after MEKi treatment, we first assessed the effect of MEKi on the expression of (phosphorylated) p-MEK1/2 and p-ERK1/2 in effector cells in the TME. We found that, although MEKi treatment of vaccinated animals significantly reduced the frequency of p-MEK1/2$^+$ and p-ERK1/2$^+$ $CD8^+$ T cells in the TME (Extended Data Fig. 1a), total and antigen-specific $CD8^+$ T cells significantly increased (Fig. 1c,d). A significant percentage of antigen-specific $CD8^+$ T cells expressed granzyme B, indicating that MEKi leads to the expansion of functional antigen-specific effector cells in the TME (Fig. 1e). Next, we found a significant decrease in $CD8^+$ T cells expressing inhibitory receptors (CTLA4, LAG3 and TIM3) (Fig. 1f–h), while an increase in CXCR3-, IL-2Rβ- and OX40-expressing activated $CD8^+$ T cells (Fig. 1i–k) in the TME of MEKi-treated mice. The expression of PD-1 on $CD8^+$ T cells was not changed in MEKi-treated vaccinated mice compared to mice treated

with vaccine alone (Fig. 1l), which is consistent with PD-1 being an activation marker[16,17]. Together, these data show that MEK inhibition enhances tumor infiltration with the effector $CD8^+$ T cells, prevents exhaustion and maintains effector $CD8^+$ T cells in an activated state.

MEKi enhances metabolic fitness in $CD8^+$ T cells by upregulating mitochondrial function.

Antitumor activity of the effector cells is associated with their metabolic fitness[6]. As the Ras–Raf–MAPK pathway plays an important role in the regulation of cell metabolism[4,18], we defined the effect of MEK1/2 inhibition on T cell metabolism. First, we looked at the mitochondrial mass in $CD8^+$ T cells in the TME, which was significantly increased in MEKi-treated vaccinated animals compared to control animals (Fig. 2a). Furthermore, ex vivo, we also found a discernibly higher number of mitochondria in pMel-1 MEKi-treated $CD8^+$ T cells (Fig. 2b). Morphologically, MEKi-treated cells had compact mitochondria with tightly packed cristae, indicating an intact redox machinery[7] and enhanced respiratory capacity[19], which was contrary to cells treated with gp100 alone, where mitochondria had diffused cristae (Fig. 2c). Accordingly, MEKi-treated $CD8^+$ T cells had a significantly higher oxygen consumption rate (OCR)/maximal respiration and spare respiratory capacity (SRC), and lower extracellular acidification rates (ECAR) (Fig. 2d). This was further confirmed by inhibition of proliferation of MEKi-treated $CD8^+$ T cells by oligomycin, an inhibitor of oxidative phosphorylation (Extended Data Fig. 1b). Together, these data demonstrated enhanced metabolic fitness and a greater reliance of MEKi-treated $CD8^+$ T cells on mitochondrial respiration. We next tested the relative contribution of glucose and fatty acids (FAs) as substrates for mitochondrial respiration in MEKi-treated $CD8^+$ T cells. We found similar glucose uptake rates, as determined by 2-NBDG (2-(*N*-(7-nitrobenz-2-oxa-1,3-diazol-4-yl) amino)-2-deoxyglucose) incorporation (Fig. 2e) and similar expression of the glucose transporter gene *Glut1* (*Slc2a1*) (Fig. 2f) in MEKi-treated $CD8^+$ T cells. These data indicate that glucose is not utilized preferentially as a substrate for energy generation following MEKi treatment of $CD8^+$ T cells. This was further confirmed by the equally reduced proliferation of MEKi-treated or untreated $CD8^+$ T cells after 2-deoxy-D-glucose (2DG) treatment, a pharmacological inhibitor of glycolysis (Fig. 2g). We next determined the status of FAO in the MEKi-treated $CD8^+$ T cells. We found increased expression of Cpt1a, a rate limiting enzyme of FAO[20], and increased uptake of BODIPY, a lipophilic probe that acts as an indicator of lipid uptake[21] (Fig. 2h,i), thus showing enhanced uptake of FAs by MEKi-treated $CD8^+$ T cells. Finally, we assessed the FA utilization in $CD8^+$ T cells after MEKi treatment by incorporation of long-chain FAs. We found a marked decrease in the palmitate-mediated OCR (Fig. 2j) and proliferation in MEKi-treated $CD8^+$ T cells upon treatment with etomoxir (Fig. 2k). In line with in vitro data, MEKi treatment of vaccinated animals significantly enhanced FA-mediated metabolism without affecting the glucose uptake rates in the $CD8^+$ T cells in the TME (Fig. 2l). Moreover, a significant increase in PGC1α, a protein involved in mitochondrial biogenesis[22] (Fig. 2l), confirms that MEK inhibition enhances metabolism in $CD8^+$ T cells.

Next, we performed deep metabolomic ($N = 356$) and lipidomic ($N = 958$) analysis of the MEKi-treated or -untreated $CD8^+$ T cells. The principal component analysis (PCA) score showed a distinct metabotype (Fig. 3a,b) with significant alterations in the intracellular levels of 25 metabolites and 144 lipids in gp100 plus MEKi versus gp100-only treated cells.

Most significant changes were found in metabolites of tricarboxylic acid (TCA) and the FA pathway (Fig. 3c,d). A pairwise analysis revealed that the glucose metabolism of $CD8^+$ T cells was not different in gp100-activated, MEKi-treated or -untreated cells (Fig. 3d), confirming that MEKi-treated cells do not utilize glucose preferentially. Treatment of $CD8^+$ T cells with gp100 alone led to an increase in lactic acid and a corresponding decrease in pyruvate compared to gp100 plus MEKi-treated cells (Fig. 3d), which corresponded well with the increased ECAR seen in gp100-only treated cells (Fig. 2d). On the other hand, the overall levels of metabolites in the TCA cycle were less in MEKi-treated cells compared to untreated cells (Fig. 3d,e), indicating a quiescent nature for these cells. In line with the palmitate utilization assay (Fig. 2j), the concentration of palmitic acid, as well as of various FA chains, was less in MEKi-treated cells (Fig. 3d,e), indicating a greater reliance of these cells on FA metabolism. These data clearly show that MEK inhibition differentially enhances the FA-mediated metabolism in $CD8^+$ T cells.

It is known that MEK1/2, ERK1/2 and cyclin D1 are involved in linking external mitogenic cues to intracellular metabolic proteins[23], including PGC1α and SIRT3 (refs. [4,24]). We found that MEK inhibition decreased the expression of p-ERK1/2 and cyclin D1 (Fig. 3f) with a corresponding increase in the expression of PGC1α (Fig. 3g), supporting the observed mitochondrial biogenesis and increased oxidative phosphorylation in $CD8^+$ T cells. Furthermore, we found that SIRT3, the NAD-dependent deacetylase sirtuin 3 that supports FAO-mediated metabolism and is downstream to PGC1α[25], was increased in $CD8^+$ T cells after MEK inhibition (Fig. 3g). Together, these results demonstrate that MEKi enhances metabolic fitness in $CD8^+$ T cells by increasing PGC1α and promoting SIRT3 and FAO-based cell respiration.

MEKi treatment induces T_{SCM} in $CD8^+$ T cells.

Enhanced metabolic fitness, high SRC and FAO are strong indicators of immune memory[20]. Accordingly, we checked the effect of MEK1/2 inhibition on memory generation in the TME. We found that CCR7, which is associated with memory[26], was upregulated (Fig. 4a), while KLRG1, low expression of which enables memory generation[27], was reduced in $CD8^+$ T cells from MEKi-treated animals (Fig. 4b). In line with these observations, we found a significant increase in the numbers of $CD62L^+CD44^+$ T_{CM} $CD8^+$ T cells (Fig. 4c). We also observed a significant increase in the numbers of $CD62L^+CD44^-$ naive $CD8^+$ T cells (Fig. 4d)[28]. However, despite a naive-like phenotype, these cells were expressing high levels of memory markers (CD95 and CCR7) (Fig. 4e). Earlier, a minimally differentiated population of T_{SCM} cells characterized by a naive-like phenotype ($CD62L^+CD44^-$) with high expression of Sca1 (ref. [29]) and lower mitochondrial potential, observed by TMRM (tetramethylrhodamine, methyl ester) incorporation[30], has been described. Indeed, we observed significantly increased numbers of $Sca1^+CD62L^+CD44^-$ and $TMRM^{lo}$ $CD62L^+CD44^-$ $CD8^+$ T cells following MEKi treatment (Fig. 4f). Furthermore, the expression of IL-2Rβ on the naive-like cells, which acts as a survival factor for lymphocytes, a further indication of stem-like characteristics[13], was significantly increased following MEKi treatment (Fig. 4g). Hence, these data indicate that MEKi treatment results in a substantial enrichment of $CD8^+$ T_{SCM} in the TME.

Further, we characterized MEKi-induced CD8$^+$ T_{SCM} cells in vitro by activating CD8$^+$ T cells with gp100 peptide in the presence or absence of MEKi (Extended Data Fig. 2a). In the absence of MEKi, a major fraction of activated CD8$^+$ T cells attained a T_{CM} phenotype (93 ± 4.5%) with only a minor fraction (6.5 ± 5.6%) staying in the naive phenotype (Fig. 4h), while the presence of MEKi resulted in a significant increase in a naive-like phenotype (CD62L$^+$CD44$^-$) (15 ± 3.2%) (Fig. 4h). However, unlike naive cells, CD62L$^+$CD44$^-$ cells in the MEKi treatment group showed high proliferative ability (Fig. 4i and Extended Data Fig. 2b), higher expression of Sca1 (Fig. 4j) and lower mitochondrial potential (Fig. 4k), besides having higher expression of memory (CD95 and CCR7) (Extended Data Fig. 2c) and activation (CXCR5 and IL-2Rβ) markers (Extended Data Fig. 2d), showing the induction of CD8$^+$ T_{SCM} cells under ex vivo conditions as well. Expression of Krupple-like factor 2 (KLF2), which is associated with increased self-renewability, prolonged survival and reduced apoptosis[31], was found to be upregulated in MEKi-treated CD8$^+$ T cells (Fig. 4l) that also showed reduced apoptosis (Fig. 4m), thus depicting T_{SCM} generation. Functionally, in accordance with earlier observations[30], MEKi-treated CD8$^+$ T cells in the naive compartment (Extended Data Fig. 2e) expressed significantly lower levels of markers associated with effector functions (IFN-γ, granzyme B and perforin-1) and exhaustion (Eomes), at both protein and messenger RNA levels (Extended Data Fig. 2f,g), confirming their T_{SCM} phenotype. We also checked if a similar T_{SCM} phenotype could be induced by other MEK1/2 inhibitors. We found a similar induction of T_{SCM} cells (Extended Data Fig. 2h) with high FA-mediated metabolism and unaltered glucose metabolism (Extended Data Fig. 2i,j) after treatment of CD8$^+$ T cells with trametinib[10]. These findings clearly indicate that activation of naive CD8$^+$ T cells in the presence of MEKi, both in vitro and in vivo, leads to induction of the T_{SCM} phenotype.

Next, we confirmed the contribution of the two MEK isoforms in the generation of the T_{SCM} phenotype. By knocking down MEK1, MEK2 or both genes in antigen-specific CD8$^+$ T cells using specific short interfering RNAs (siRNAs) (Extended Data Fig. 3a,b), we found that knockdown of both MEK1 and MEK2 led to a significant enrichment of naive-like CD62L$^+$CD44$^-$ (Extended Data Fig. 3c) and TMRM^{lo} CD8$^+$ T cells (Extended Data Fig. 3d). However, the knockdown of MEK1 or MEK2 alone was not sufficient to induce T_{SCM} cells (Extended Data Fig. 3e), confirming that inhibition of both isoforms is necessary for enrichment of the T_{SCM} phenotype.

MEKi-induced T_{SCM} in CD8$^+$ T cells are distinct from T_{CM} and T_{naive} cells.

We next tested the effect of MEK1/2 inhibition on the generation of T_{SCM} cells in human CD8$^+$ T cells. In agreement with mouse data, MEK1/2 inhibition of human CD8$^+$ T cells led to a significant increase in the numbers of CD45RA$^+$CCR7^{hi}CD62L$^+$CD95$^+$ CD8$^+$ T cells (Fig. 5a and Extended Data Fig. 4a) with low mitochondrial potential (Fig. 5b,c). To confirm that T_{SCM} (CD45RA$^+$CCR7$^+$CD95$^+$) cells are distinct from T_{naive} (CD45RA$^+$CCR7$^-$CD95$^-$) and T_{CM} (CD45RA$^-$CCR7$^+$) cells, we examined the whole-genome and loci-specific methylation profiles of various FACS-sorted human CD8$^+$ T cell phenotypes (Extended Data Fig. 4a). A heat map analysis of the top 3,000 CpGs, selected in an unbiased manner from the whole epigenome, conclusively showed a distinct methylation profile of MEKi-induced T_{SCM} cells compared to T_{naive} and T_{CM} cells induced with or

without MEKi (Fig. 5d). We also quantified the number of differentially methylated regions (DMRs) among the MEKi-induced T_{SCM} versus freshly isolated naive, bona fide T_{SCM}, T_{CM} and T effector memory (T_{EM}) $CD8^+$ T cells. These data show that the MEKi-T_{SCM} and freshly isolated bona fide T_{SCM}, as characterized recently[32], are the most closely related as they have the least number of DMRs (Extended Data Fig. 4b). To support these claims, we further compared the CpG DNA methylation of key genes dynamically regulated during T cell memory development[14] (*Ifng*, *Prf1* and *Tcf7*) across three cell populations. DNA methylation of CpG sites in *Ifng* and *Prf1* loci in T_{SCM} cells, when compared to T_{CM} cells, contained higher CpG methylation (suggesting less transcriptional activity) (Fig. 5e,f and Extended Data Fig. 4c), while the *Tcf7* locus demonstrated a higher degree of unmethylated CpG sites, indicative of a more open, transcriptionally active region (Fig. 5g and Extended Data Fig. 4c). The methylation at these gene loci in T_{SCM} cells was also distinct from T_{naive} cells, which had a relatively similar degree of CpG demethylation in the *Tcf7* locus, and demonstrated nearly full methylation of *Ifng* and *Prf1* loci, which is reflective of their stem-like characteristic (*Tcf7*) and lack of effector programming (*Ifng*, *Prf1*). Hence, as shown earlier[28], the T_{SCM} cells generated after MEKi possessed the characteristics of an intermediate state between T_{naive} and T_{CM} cells (Fig. 5d–g and Extended Data Fig. 4b,c). Further, the multipotency/plasticity, proliferation indices and the self-renewal capacity have been shown to functionally differentiate T_{SCM} and T_{CM} populations[28]. We assessed and compared the plasticity of these cells by utilizing a DNA methylation-based multipotency index[32] with our MEKi-induced T_{SCM} samples to that of T_{naive}, T_{SCM}, and T_{CM} cells obtained from healthy donors (HD). We found a similar plasticity score between MEKi-induced and bona fide T_{SCM} cells (Fig. 5h). Furthermore, the MEKi-T_{SCM} plasticity score was found to be lower than that of T_{naive} (HD or IL-2) and higher than T_{CM} cells (HD, activated or MEKi-treated) (Fig. 5h). We next confirmed these methylation-based multipotency indices by checking the ability of MEKi-T_{SCM} versus T_{CM} populations to produce various cell types. In accordance with earlier observations[13,28], T_{SCM} cells were found to have higher multipotency as well as proliferation indices compared to T_{CM} cells (Fig. 5i). These results confirm that $CD8^+$ T cells, when treated with MEKi, become T_{SCM} cells having high self-renewal potential, multipotency and higher proliferation ability, and are distinct from T_{naive} and T_{CM} cells[13,28].

MEKi induces T_{SCM} by inhibiting cell cycle progression and differentiation during TCR-mediated cell priming.

It is crucial to determine the state of $CD8^+$ T cells that can generate the T_{SCM} phenotype. In vitro, we found that the $CD8^+$ T cells that were preactivated with gp100 failed to develop the T_{SCM} phenotype upon MEKi treatment (Fig. 6a,b, last bar). On the other hand, T_{SCM} cells were robustly generated when naive $CD8^+$ T cells were treated with MEKi while being challenged with a cognate antigen (Fig. 6a,b; third versus last bar), strongly suggesting that naive and not preactivated $CD8^+$ T cells can be reprogrammed into T_{SCM} with MEK inhibition.

Since MEK inhibition decreased cell proliferation (Fig. 2g,k) and cyclin D1 expression (Fig. 3f), we next determined the effect of MEKi on cell cycle progression and differentiation. We found a delay in the cell cycle progression with an increased accumulation of cells in earlier

generations of cell division (Fig. 6c), which nonetheless were properly activated (Extended Data Fig. 2d), as was confirmed by the expression of p-PI3K and p-Akt molecules in these cells (Fig. 6d). These results indicate that MEK inhibition does not affect PI3K- or Akt-mediated $CD8^+$ T cell activation. Hence, MEKi inhibits the cell cycle in early phases, while allowing proper antigen-mediated activation to generate naive-like antigen-experienced T_{SCM} cells. Indeed, the analysis of different generations of proliferation clearly showed that generations 1 and 2 had increased numbers of T_{SCM} cells ($Sca1^{hi}$) when compared to generation 3 after MEKi treatment (Fig. 6e). Furthermore, without MEKi, the majority of the cells differentiated to T_{EM} while MEK inhibition enriched the T_{SCM} in early generations, inhibiting their further differentiation into T_{CM} and T_{EM} (Fig. 6f). This indicates that $CD8^+$ T cell activation and its commitment to the cycle of differentiation are independent events. Hence, MEK1/2 inhibition holds $CD8^+$ T cells in the earliest stages of the differentiation cycle without affecting the effector or activation status of the cells.

MEKi-mediated inhibition of cell cycle progression and metabolic enhancement is necessary for T_{SCM} generation.

We found that MEKi inhibits cell cycle progression (Figs. 3f and 6c) and enhances the metabolic fitness of $CD8^+$ T cells (Fig. 3g). We next asked if both inhibition of cell cycle progression and metabolic enhancement are necessary for MEKi-mediated T_{SCM} generation. For this, we first inhibited ERK1/2 and cyclin D1 and found that inhibition of these molecules during cellular activation resulted in a significant induction of the T_{SCM} phenotype in $CD8^+$ T cells (Fig. 7a). These data suggest that a delay in cell cycle progression is required for T_{SCM} generation. Next, we checked the effect of absence of PCG1α or SIRT3 on MEKi-induced T_{SCM} generation by inhibiting PGC1α or using *Sirt3* knockout cells. We found a significant reduction in the numbers of MEKi-induced T_{SCM} cells generated after inhibition of PGC1α or in *Sirt3* knockout $CD8^+$ T cells (Fig. 7b,c). Next, we blocked FAO using etomoxir and found a complete abrogation of T_{SCM} generation (Fig. 7d), establishing FAO as a critical factor for MEKi-mediated T_{SCM} generation. These results show that inhibition of cell cycle progression and FAO-mediated cellular metabolism are critical for MEKi-induced T_{SCM} generation. Next, to check the relative contribution of inhibition of cell cycle and enhancement of metabolism in induction of T_{SCM} cells, we treated $CD8^+$ T cells with MEKi (for blocking the cell cycle) and PGC1αi (to limit the cell metabolism) and determined the generation of T_{SCM} cells. We found that, although the number of T_{naive} cells ($CD62L^+CD44^-$) were similar in gp100 plus MEKi versus gp100 plus MEKi plus PGC1αi groups (18.3 ± 0.11% versus 19.5 ± 0.94%, respectively) (Extended Data Fig. 4d), T_{SCM} cells ($Sca1^+CD62L^+CD44^-$) were generated in significantly higher numbers in the gp100 plus MEKi group (11.9 ± 0.41%) and not in the gp100 plus MEKi plus PGC1αi group (6.6 ± 0.44%) group (Fig. 7b). These data show that a concerted effect of delay in cell cycle progression and enhanced metabolism during antigen-mediated cell activation is required for T_{SCM} generation.

MEKi-induced T_{SCM} $CD8^+$ T cells have higher recall response and superior antitumor activity after ACT of tumors.

T_{SCM} cells are known to have strong recall responses that are crucial for their effective antitumor activity, especially after ACT[33]. Therefore, we next determined the recall response

and antitumor activity of MEKi-induced T_{SCM} cells in an ACT tumor model. We found that, compared to untreated cells, in vitro MEKi-treated $CD8^+$ T cells had an approximately fivefold higher effector cell recall response and higher T_{SCM} cell number (Fig. 8a). Furthermore, higher levels of IFN-γ and granzyme B were also observed in MEKi-treated $CD8^+$ T cells after antigenic rechallenge (Fig. 8b). These results indicate the potentially stronger antitumor effect of MEKi-treated $CD8^+$ T cells when used in ACT. Hence, we adoptively transferred in vitro gp100 plus MEKi-activated $CD8^+$ T cells into B16F10 melanoma-bearing mice and evaluated the tumor growth rates, mouse survival and frequency of transferred cells in the TME at days 22 and 30 after transfusion. First, we ascertained the cell engraftment postinfusion and found that the two cell populations (MEKi treated or untreated) had equal levels of engraftment in spleen and tumors (Extended Data Fig. 5a). Mice that received MEKi-treated $CD8^+$ T cells had a significantly higher antitumor response (Fig. 8c) and prolonged survival (Fig. 8d) compared to $CD8^+$ T cells activated with gp100 alone. To confirm the contribution of MEKi-T_{SCM} cells in antitumor activity after ACT, we depleted the $CD62L^+CD44^-$ cells and transfused only $CD62L^+CD44^+$ T cells from gp100 and gp100 plus MEKi-activated groups. We found that, although in the gp100-only activated group there was no discernible difference in the antitumor activity whether or not $CD62L^+CD44^-$ cells were present, MEKi-treated $CD8^+$ T cells demonstrated a significantly reduced antitumor activity if $CD62L^+CD44^-$ cells were depleted (Fig. 8c,d). These data indicate that MEKi-induced T_{SCM} played a major role in antitumor activity of $CD8^+$ T cells, establishing MEK1/2 inhibition as a critical factor for T_{SCM} generation and enhanced antitumor activity. The antitumor activity of MEKi-treated T_{SCM}-depleted $CD8^+$ T cells was still higher than gp100-only treated cells (Fig. 8c,d), indicating that MEKi also enhanced the antitumor activity of T_{CM} cells. This enhanced antitumor activity of MEKi-induced T_{CM} cells could be due to differential DNA methylation of key genes, as potentially demonstrated by increased demethylation of *Ifng* and *Prf1* genes in human MEKi-treated compared to non-MEKi-treated T_{CM} cells (Extended Data Fig. 5b). Together, these results demonstrate that MEKi not only results in increased T_{SCM} generation, but also enhances the functionality of T_{CM} cells.

Furthermore, we established the longevity and activation status of the T_{SCM} cells postinfusion. We found that MEKi-treated $CD8^+$ T cells were present with higher frequencies in the TME, at both day 22 (Extended Data Fig. 5c) and day 30 (Fig. 8e) after cell transfer, compared to gp100-treated cells, which were collected either at day 22 or at the time the mice were killed (when tumor volume reached 1.5 cm^3). MEKi-treated $CD8^+$ T cells showed equal expression of CD62L, with a significantly lower expression of CD44 compared to non-MEKi-treated cells at day 30 (Fig. 8f), showing maintenance of memory phenotype in MEKi-treated cells compared to non-MEKi-treated cells[34].

These results demonstrate that MEKi-treated $CD8^+$ T cells show strong effector functions during recall responses and that MEKi-induced T_{SCM} cells contribute substantially to these responses. Reduced levels of mTORC1 are associated with memory generation[35,36] while upregulated mTORC1 is required for generation of robust effector functions[37]. We observed a reduction in the levels of p-mTORC1 in MEKi-treated $CD8^+$ T cells during initial cell activation and T_{SCM} generation, with an upregulated expression of p-mTORC1 in MEKi-treated $CD8^+$ T cells following antigenic rechallenge (Extended Data Fig. 5d), showing that,

initially, mTORC1 is inhibited reversibly and available for recall responses. In conclusion, these results indicate that MEKi treatment induces $CD8^+$ T_{SCM} cells by a concerted effect on cell cycle, metabolism and cell activation, which have superior antitumor activity with prolonged persistence in the TME and ACT settings (Extended Data Fig. 5e).

Discussion

We report, an effective strategy for reprograming naive $CD8^+$ T cells into T_{SCM} through inhibition of MEK1/2 signaling. We found that MEK1/2 inhibition generates exceedingly functional $CD8^+$ T_{SCM} cells with high FAO-mediated metabolic fitness, self-renewability, high proliferation, multipotent capacity and antigen recall responses. This resulted in generation of potent effector $CD8^+$ T cells with prolonged survival and superior antitumor activity. Thus, utilizing MEK1/2 SMIs represents a major opportunity to enhance the efficacy of immunotherapeutic strategies. This includes a strategy to enhance the antitumor efficacy of ex vivo expanded or engineered T cells for ACT; as well as in vivo use of these inhibitors to augment the effects of immune modulatory agents, especially those that induce, stabilize and enhance T cell memory[38].

T_{SCM} are cells that phylogenetically reside between naive and memory T cell populations[13]. Indeed, MEKi-induced T_{SCM} cells show similar DNA methylation profiles to bona fide T_{SCM} from HD[14] that is intermediate between T_{naive} and T_{CM} cells. Moreover, in line with the functional characteristics of bona fide T_{SCM} cells[30,39,40], antigen rechallenged MEKi-induced T_{SCM} cells showed self-renewal capacity, and higher proliferative and multipotency indices. These characteristics provide T_{SCM} cells with a therapeutic advantage over T_{CM} cells, since the T_{CM} pool wanes over time[41]. Interestingly, like T_{SCM}, MEKi-T_{CM} (which could be generated from T_{SCM} or directly under the influence of MEKi) were functionally superior to the non-MEKi-induced T_{CM} cells, as MEKi-T_{CM} had higher demethylation at *Ifng* and *Prf1* gene loci, reflecting their stronger antitumor effects after ACT. It is important to note that enhanced antitumor activity of MEKi-treated $CD8^+$ T cells was critically dependent on MEKi-T_{SCM} cells, as their depletion resulted in a significant loss of antitumor response.

Further, T_{SCM} cells are generated only when MEK1/2 is inhibited during initial antigen activation of naive $CD8^+$ T cells. The fact that the TME supports the infiltration, activation and differentiation of naive $CD8^+$ T cells[42,43] allows generation of MEKi-induced T_{SCM} cells. However, since resident memory T cells can traffic to the TME after reactivation[44], MEK inhibition may also generate T_{SCM} cells outside the TME. We believe that MEK1/2 inhibition in naive $CD8^+$ T cells during initial antigen priming allows TCR-mediated cell activation that, coupled with cell cycle inhibition, results in the accumulation of antigen-experienced $CD8^+$ T cells in early phases of differentiation. In this context, a recent study shows that a gradual decrease in cell cycle is crucial for generation of memory[45]. Additionally, MEK inhibition that leads to increased PGC1α-mediated mitochondrial biogenesis and functionality, confirmed by compact mitochondria and enhanced FAO results in enhanced metabolic fitness of cells and generation of memory. Coupling of these two processes (decreased cell cycle and enhanced metabolism) results in the generation of the T_{SCM} phenotype, which was evident by nongeneration of T_{SCM} cells in $CD8^+$ T cells

treated with gp100 (increased cell cycle and PGC1α); gp100 plus PGC1αi (increased cell cycle and decreased metabolism); gp100 plus MEKi plus PGC1αi (decreased cell cycle and metabolism) compared to gp100 plus MEKi (decreased cell cycle and increased metabolism). This conclusively shows that neither of the two phenomena alone, that is, delay in cell cycle progression or enhanced metabolism, are sufficient for T_{SCM} generation. Rather, the concerted effect of both pathways during antigen-mediated cell activation is required. Moreover, we also found a transient reduction in mTORC1 activity by MEK1/2 inhibition during initial cell priming, which is known to increase FAO and generate memory[35,36]. An intact PI3K–Akt and mTORC1 signaling is required for cell reactivation, proliferation and generation of effector cells[36,37], signaling events that are also observed after reactivation of MEKi-treated $CD8^+$ T cells and which facilitate robust recall responses. Together, these observations indicate that MEK1/2 signaling may be deterministic for commitment of $CD8^+$ T cells onto the path of cell cycle differentiation independent of TCR-mediated cell activation, ultimately deciding the terminal phenotype that will be generated after cell activation.

As T_{SCM} cells produce highly activated and less exhausted effector $CD8^+$ T cells upon restimulation with the cognate antigen, MEKi-treated animals had higher number of well-activated (higher CXCR3, IL-2Rβ, OX40), unexhausted (lower CTLA4, TIM3, LAG3) effector cells in the TME compared to non-MEKi-treated mice, leading to a significantly enhanced antitumor immune response. These results also help to explain earlier anecdotal observations that MEK inhibition during initial antigenic stimulation of $CD8^+$ T cells inhibits cell proliferation and production of IFN-γ in vitro, while generating robust effector function in the TME[9,10]. Our data clearly show that MEK1/2 inhibition does not prevent initial T cell priming[9], which is crucial for generation of antitumor responses[46]. Rather, MEKi induces T_{SCM} cells that tend to have lower expression of activation markers on $CD8^+$ T cells[28]. Furthermore, these MEKi-treated cells possess significantly improved recall response, which explains their robust effector functions in the TME as observed by others[9].

Since T_{SCM} have crucial functions in several biological processes, multiple redundant pathways are expected to regulate their generation. Indeed, T_{SCM} cells can be induced after activation of Wnt/β-catenin signaling or after chronic lymphocytic choriomeningitis virus infection in a TCF1-dependent manner in $CD8^+$ T cells[47,48]. Here, we demonstrate a mechanism of T_{SCM} induction in $CD8^+$ T cells by MEK1/2 inhibition and propose a model. According to this model, TCR-mediated cell activation prepares the cell for division, while temporary MEK1/2 inhibition decreases the levels of activated ERK1/2 and cyclin D1, resulting in delayed cell cycle progression. This increases PGC1α/SIRT3, enhancing FAO-mediated metabolic fitness, as shown by metabolic analysis, and facilitating T_{SCM} generation. Notably, although MEKi reduces T cell proliferation, it does not affect antigen-mediated cell activation. This model provides a comprehensive understanding of the mechanisms of MEK inhibition with respect to cell cycle progression, metabolic reprogramming and antigen-mediated cell priming and activation, leading to T_{SCM} generation.

In conclusion, these results demonstrate the reprogrammability of $CD8^+$ T cells into stemness fate by inhibiting MEK1/2. This may have important physiological implications,

since cytokines such as IL-15 and IL-7, which are known to enhance immune memory[49], might induce T_{SCM} under physiological conditions by limiting the MEK activity. This, in turn, would help to sustain the memory pool for durability of the response, especially against infectious agents. Furthermore, MEK inhibition forms a pharmacologically feasible method that can be used to enhance different immune therapeutic approaches, including combination with priming agents, immune modulators or enhancing the efficacy of cellular therapies. In addition, unlike targeting the Wnt pathway, MEKi has important clinical implications, since SMIs of MEK are already approved by the US Federal Drug Administration and are in use for cancer treatment (NCT02407405).

Methods

Mice and cell culture.

Four-to-six-week-old C57BL/6J mice (wild type) and *Sirt3* knockout mice on C57BL/6J background were purchased from Jackson Laboratory. In-house-bred pMel-1 mice [B6.Cg-Thy1^a/Cy Tg (TcraTcrb)8Rest/J], which carry a rearranged TCR transgene (*Vβ13*) specific for the mouse homolog (*pmel-17*) of human *gp100* (ref. [50]), with transgenic $CD8^+$ T cells having a melanoma-gp100 peptide-specific TCR were used as outlined in various experiments. Animals had free access to water and food. All experiments were performed under protocols approved by the Augusta University Georgia Cancer Center and Georgetown University Institutional Animal Care and Use Committee (IACUC). Cancer cell lines used in the present study included TC-1 (kindly provided by T.-C. Wu, Johns Hopkins University)[51] and B16F10 melanoma (obtained from the American Type Culture Collection (ATCC)). Cells were cultured as described earlier[46]. Cell lines were routinely tested for absence of any contamination, including mycoplasma, by microscopic evaluation and PCR-based methods. Human peripheral blood mononuclear cells (PBMCs) from healthy donors were purchased from Hemacare BioResearch Products & Services (catalog no. M009C-2). Primary murine $CD8^+$ T cells, as well as human $CD8^+$ T cells, were isolated by fluorescence-activated cell sorting (FACS) and, in some cases, by negative selection using magnetic beads (Miltenyi Biotec), and cultured in RPMI 1640 medium supplemented with 10% FBS, 2 mM glutamine, 10 mM HEPES and 55 μM β-mercaptoethanol. Purity of all the cell populations was greater than 95%.

Tumor establishment and mice treatment.

C57BL/6J mice were injected with 70,000 TC-1 cells per mouse or 0.1×10^6 B16F10 cells per mouse in the right flank. Treatment in respective groups was started when tumors reached an average size of approximately 0.075 cm^3. MEKi treatment was performed using selumetinib (AZD6244, ARRY-142886) obtained from AstraZeneca under a Materials Transfer Agreement. Mice were dosed orally for 15 d starting at day 6–7 (at an average tumor size of 0.04–0.06 cm^3) at a dose of 10 mg kg^{-1}. For vaccination, TC-1-specific E7-peptide (a nine amino acid peptide, RAHYNIVTF; 100 μg per mouse per 100 μl; Celtak Bioscience) or B16-specific $gp100_{25–33}$ nonamer peptide (KVPRNQDWL; 100 μg per mouse per 100 μl; AnaSpec)[52] were used. Both the vaccines were mixed with a small 13-mer nonnatural pan-HLA DR-binding epitope (PADRE; aK-Cha-VAAWTLKAAa, where ‘a’ is D-alanine, and ‘Cha’ is L-cyclohexylalanine, T helper epitope, 20 μg per

mouse; Celtak Bioscience) and QuilA (adjuvant, 10 μg per mouse; Brenntag). For survival and therapy experiments mice were vaccinated three times, starting at day 12, while for immune response experiments mice were vaccinated twice with a one-week interval between vaccinations. In some experiments, TC-1 tumors were implanted as above and 2–3 days after the second vaccination tumors were collected and processed as described below. Tumors were measured every 3–4 days using a digital vernier caliper, and the tumor volume was calculated using the formula: $V = L \times W^2/2$, where V is tumor volume, L is the length of the tumor (longer diameter) and W is the width of the tumor (shorter diameter). Mice were monitored for tumor growth and survival. Mice were killed when the tumor volume reached 1.5 cm^3.

Tumor collection and sample preparation.

Two-to-three days after the second vaccination, mice in the various groups were killed and tumors were collected. Samples were processed using a gentleMACS dissociator and the solid tumor homogenization protocol, as suggested by the manufacturer (Miltenyi Biotec).

Antibodies and reagents.

The Live/Dead Fixable Near-IR Dead Cell Stain Kit (catalog no. L34976) and CellTrace Violet (VCT) Cell Proliferation Kit (catalog no. C34557) were obtained from ThermoFisher Scientific. The fluorochrome-labeled anti-mouse antibodies used for flow cytometry measurements in vitro and in vivo were: V450-CD45 (1:200, clone 30-F11, catalog no. 103125; eBioscience); TxRd-CD3 (1:200, clone 145–2c11, catalog no. 562286; BD Biosciences); Alexa Fluor 700-CD8a (1:200, clone 53–6.7, catalog no. 557959; BD Biosciences); V450-CD8 (1:200, clone 53–6.7, catalog no. 560469; BD Biosciences); PE-Annexin V (1:200, catalog no. 556421; BD Biosciences); FITC-IFN-γ (1:100, clone xmg1.2, catalog no. 557724; BD Biosciences), Alexa Fluor 700-CD62L (1:200, clone MEL-14, catalog no. 560517; BD Biosciences); FITC-CD44 (1:200, clone IM7, catalog no. 553133; BD Biosciences); PE-PD-1 (1:200, clone 29F.1A12, catalog no. 135206; BioLegend); APC-Ki-67 (1:200, clone SolA15, catalog no. 17–5698-82; eBioscience); PE-phospho-Akt (pS473) (1:10, clone M89–61, catalog no. 560378; BD Biosciences); FITC-Sca1 (1:200, clone D7, catalog no. 11–5981-82; Invitrogen); APC-Granzyme B (1:100, clone GB11, catalog no. 515406; BioLegend); FITC-Perforin (1:100, clone eBioOMAK-D, catalog no. 11–9392-82; Invitrogen); APC-KLRG1 (1:200, clone 2F1, catalog no. 561620; BD Biosciences); PE-CTLA4 (1:200, clone UC10–4F10–11, catalog no. 553720; BD Biosciences); APC-LAG3 (1:200, clone eBioC9B7W, catalog no. 17–2231-82; Invitrogen); PE-TIM3 (1:200, clone B8.2C12, catalog no. 134004; BioLegend); FITC-CXCR3 (1:200, clone CXCR3–173, catalog no. 11–1831-80; Invitrogen); APC-CXCR5 (1:200, clone SPRCL5, catalog no. 17–7185-82; Invitrogen); APC-CCR7 (1:200, clone 4B12, catalog no. 17–1971-63; eBioscience); PE-IL-2Rβ (1:200, clone TM-B1, catalog no. 553362; BD Biosciences); FITC-CD95 (1:200, clone Jo2, catalog no. 561979; BD Biosciences); APC-OX40 (1:200, clone OX-86, catalog no. 119414; BioLegend); APC-Eomes (1:200, clone Dan11mag, catalog no. 14–4875-82; Invitrogen); FITC-Bcl2 (1:200, clone 10C4, catalog no. 11–6992-42; Invitrogen); APC-Thy1.1 (1:200, clone HIS51, catalog no. 17–0900-82; eBioscience); V450-Thy1.1 (1:200, clone HIS51, catalog no. 48–0900-82; Invitrogen); APC-p-MEK1 (1:20, clone 25/MEK1, catalog no. 560101; BD Biosciences); PE-p-MEK2

(1:20, clone 96/MEK2, catalog no. 560388; BD Biosciences); PE-p-MEK1/2 (1:20, clone O24–836, catalog no. 562458; BD Biosciences); FITC-p-ERK1/2 (1:20, clone MILAN8R, catalog no. 53–9101-42; Invitrogen); PE-Cyclin D1 (1:20, clone DCS-6, catalog no. MA5–28534; Invitrogen); AF647-PGC1α (1:20, clone F/P:1.930, catalog no. NBP1–04676AF647; Novus); FITC-SIRT3 (1:20, clone SIR3, catalog no. SIR3-FITC; FabGenniX); FITC-p-PI3K (1:100, clone PI3KY458–1A11, catalog no. MA5–28026; Invitrogen).

The fluorochrome-labeled anti-human antibodies used for flow cytometry measurements were: APC-Cy-CD3 (1:200, clone SK7, catalog no. 557832; BD Biosciences); PECF594-CD8 (1:200, clone RPA-T8, catalog no. 562282; BD Biosciences); APC-CD45R0 (1:200, clone UCHL1, catalog no. MA1–19782; Invitrogen); FITC-CD45RA (1:200, clone HI100, catalog no. 555488; BD Biosciences); FITC-CD95 (1:200, clone DX2, catalog no. 556640; BD Biosciences); AF700-CCR7 (1:200, clone 150503, catalog no. 561143; BD Biosciences); PE-CD62L (1:200, clone DREG56, catalog no. 555544; BD Biosciences).

FITC-E7 (1:50, catalog no. JA2195-FITC) and APC-gp100 (1:50, catalog no. WB2158-APC) dextramers were obtained from Immudex. $CD8^+$ enrichment kits (Miltenyi Biotec) were used according to the manufacturer's instructions. Antibodies used for cell activation were: anti-mouse CD3 (5 μg ml^{-1}, clone 145–2C11, catalog no. 553057; BD Biosciences) and CD28 (2.5 μg ml^{-1}, clone 37.51, catalog no. 553294; BD Biosciences); and anti-human CD3 (5 μg ml^{-1}, clone OKT3, catalog no. 317302; BioLegend) and CD28 (2.5 μg ml^{-1}, clone CD28.2, catalog no. 302902; BioLegend).

Anti-mTORC1 (1:1,000, clone 7C10, catalog no. 2983T) and anti-p-mTORC1 (1:1,000, clone 7C10, catalog no. 2983T) for the immunoblot were obtained from Cell Signaling Technology, while anti-β-actin (anti-mouse) was purchased from Sigma (1:1,000; clone D9C2, catalog no. 5536T). Anti-mouse (1:1,000, catalog no. 7076S) and anti-rabbit (1:1,000, catalog no. 7074P2) horseradish peroxidase (HRP)-labeled secondary antibodies were obtained from Cell Signaling Technology.

Cell activation, drug treatment and adoptive transfer.

FACS-sorted Thy1.1 $CD8^+$ T cells from pMel-1 mice were activated with gp100 peptide (KVPRNQDWL; 1 μM per 10^6 cells per ml) either alone or in combination with MEKi (1,000 nM) in T cell medium supplemented with 30 international units (IU) of IL-2 for 48 h unless otherwise stated. In a few experiments, another MEK inhibitor, trametinib (from Selleckchem) was used at a concentration of 35 nM. For ACT experiments, $CD8^+$ T cells from pMel-1 mice were activated with gp100 peptide with and without MEKi for 48 h followed by transfer (1×10^6 cells per mouse) into 9-day-old B16F10 melanoma-bearing mice that were treated with cytoxan (2 mg per mouse) at day 8. In a few groups, $CD62L^+CD44^-$ cells were depleted by FACS sorting and transferred into tumor-bearing mice. Sorted cells were rested for 2–3 h in T cell medium at 37 °C/5% CO_2. Tumor growth and survival of mice were monitored. From another set of experiments, tumors from variously treated mice were collected at two time points. At day 22 after transfer, tumors were collected from mice that received gp100 versus gp100 plus MEKi-treated cells. At day 30, mice that received gp100 plus MEKi-treated cells were killed and their tumors were processed to determine the numbers of adoptively transferred cells by gating upon

Thy1.1 cells. However, in gp100-only-treated groups, mice were euthanized as and when their tumors reached a volume of 1.5 cm^3. These tumors were prepared into a single-cell suspension, which was stored at −80 °C until processed for FACS analysis. The frozen tumor samples from control mice were processed at day 30 along with tumors of mice that received gp100 plus MEKi-treated cells. In one separate experiment, the rate of T cell engraftment in tumors and spleen was established 48 h after T cell infusion. For this, tumors and spleens were collected from mice that received gp100 or gp100 plus MEKi-treated cells versus the respective cells cultured after FACS depletion of T_{SCM} cells. Tumor and spleen samples were analyzed by FACS by gating upon Thy1.1 cell population. In a few experiments, FACS-sorted $CD8^+$ T cells from spleen of *Sirt3* knockout mice were activated with plate-bound anti-CD3 (5 μg ml^{-1}) and anti-CD28 (2.5 μg ml^{-1}) in IL-2 (30 IU ml^{-1})-containing media for 72 h followed by FACS analysis for various markers. In a few experiments, to estimate the antigen recall responses, pMel-1 $CD8^+$ T cells were activated with gp100 or gp100 plus MEKi for 48 h, as detailed above. After incubations cells were washed and rested overnight in IL-2 (30 IU ml^{-1}) medium followed by addition of gp100 (1 μM ml^{-1}) and further incubation for 48 h. Postincubation cells were processed for FACS staining or western blot analysis as explained above. In some experiments, cells were sorted into T_{SCM} and T_{CM} phenotypes 72 h after cell activation and treatment with MEKi. After activation of cells for an additional 24 h, proliferation and differentiation of cells into different phenotypes (T_{SCM}, T_{CM} and T_{EM}) was determined by flow cytometry.

For evaluation of T_{SCM} characteristics in human $CD8^+$ T cells, $CD8^+$ T cells were isolated from normal human PBMCs by FACS sorting and activated in the presence or absence of MEKi, by plate-bound anti-human anti-CD3 and soluble anti-CD28, for 72 h. Postactivation cells were gated upon $CD8^+$ T cell population and various characteristics were investigated as described in the Results. In some experiments, cells were sorted into T_{naive}, T_{SCM} and T_{CM} phenotypes 72 h after cell activation and treatment with MEKi, and the methylation status at CpG of different gene loci was determined as described below.

Loci-specific methylation analysis.

Genomic DNA was bisulfite-treated using the EZ DNA Methylation gold kit (Zymo Research) to facilitate discrimination of methylated versus nonmethylated cytosines by sequencing. The bisulfite-modified DNA was amplified by PCR with locus-specific primers (see below) and DNA was extracted using the Gel DNA Recovery Kit (Zymo Research). The PCR amplicon was cloned into a pGEM-T cloning vector (Promega) and transformed into XL10-Gold ultracompetent bacteria (Agilent Technologies). Individual bacterial colonies were grown for 20 h at 37 °C on LB agar supplemented with 100 mg l^{-1} ampicillin, 80 mg l^{-1} X-gal and 20 mM IPTG. White, transformed colonies were selected and subcultured into LB medium supplemented with 100 mg l^{-1} ampicillin for 20 h at 37 °C. Cloning vectors were purified using the DirectPrep 96 MiniPrep kit (Qiagen) and the genomic insert was subsequently sequenced. Sequences were analyzed using Quantification tool for Methylation Analysis (QUMA) software and plotted in GraphPad Prism. Primer set information: *Ifng*: forward: GATTTAGAGTAATTTGAAATTTGTGG, reverse: CCTCCTCTAACTACTAAT ATTTATACC; *Prf1*: forward: GTGTGATTTATGAGATATGATGTTATATG,

reverse: CCACTTCCTACTCAACCTACATCCCAC; *Tcf7*: forward: AGGGGAGT TGTTGTTGATTGTA, reverse: TCCACAACAACTCAACCCTAAAAA.

Whole-genome bisulfite sequencing (WGBS) and DNA methylation-based T cell multipotency index.

WGBS was performed as previously described[14,32]. Briefly, genomic DNA was bisulfite-treated using the EZ DNA Methylation gold kit (Zymo Research). Subsequently, the bisulfite-modified DNA underwent sequencing library generation using the EpiGnome kit (Epicentre) as per manufacturer's instructions. Bisulfite-modified DNA libraries were sequenced using an Illumina HiSeq system. Sequencing data were aligned to the HG19 genome using BSMAP v.2.74 software[53]. Differential methylation analysis of CpG methylation among the datasets was determined with a Bayesian hierarchical model to detect regional methylation differences with at least three CpG sites[54].

The T cell multipotency index was used as previously described[32]. Briefly, a supervised analysis of the methylomes from naive and HIV-specific $CD8^+$ T cells identified 245 hypomethylated CpG sites, which were then used as input to a one-class logistic regression to calculate the multipotency index. The multipotency signature was applied to the sample WGBS datasets in which scores were calculated as the dot product between the DNA methylation value and the signature. The score was converted into the (0, 1) range in which multipotency values closer to 1 demonstrate a more naive-like cell.

Flow cytometry analyses.

To analyze the production of IFN-γ by $CD8^+$ T cells, cells treated in vitro were plated at a density of 2×10^6 cells per well in a 48-well plate and incubated in T cell medium containing 50 ng ml^{-1} of phorbol 12-myristate 13-acetate (catalog no. P1585), 750 ng ml^{-1} of ionomycin and 10 μg ml^{-1} of brefeldin (catalog no. B5936–200UL). Cells were incubated for 4 h at 37 °C with 5% CO_2 followed by FACS staining to detect IFN-γ and other cell markers. A total of $1–2 \times 10^6$ cells per sample were stained for Live/Dead staining followed by fixation and permeabilization. For IFN-γ staining, BD Cytofix/Cytoperm (catalog no. 51–2090KZ) and BD Perm/Wash (catalog no. 51–2091KZ) buffer set were used according to the manufacturer's instructions (BD Pharmingen). $CD8^+$ T cells from tumor samples were stained similarly. Data acquisition was performed on a BD LSR II flow cytometer using the software FACS Diva v.9.0. Results were analyzed using FlowJo software (TreeStar). MitoFM, a green-fluorescent mitochondrial stain, which localizes to mitochondria and TMRM, the cell-permeant, cationic, red-orange fluorescent dye that is readily sequestered by active mitochondria and has been used for estimation of mitochondrial potential, was used as described previously[30]. Glucose uptake assay was performed using 2-NBDG. All reagents were used as per the manufacturers' instructions. In a few experiments, the lipid profile of the activated cells was performed by BODIPY incorporation. For this, pMel-1 $CD8^+$ T cells were activated with or without MEKi for 48 h followed by surface staining as explained above. Cells were then washed and resuspended in 500 μl of BODIPY (493/503) prepared at a concentration of 0.5 μg ml^{-1} in PBS. Cells were stained for 15 min at 20 °C followed by washing and final suspension in PBS. $CD8^+$ T cells from tumor samples were stained similarly for MitoFM, BODIPY, 2-NBDG, PGC1α, p-MEK1/2, p-ERK1/2

and inhibitory, costimulatory and memory markers, and analyzed by flow cytometry. In a few experiments, variously treated cells were processed for annexin V staining to check the extent of apoptosis. For this, collected cells were surface stained for various markers as detailed above, followed by annexin V staining in annexin binding buffer (ABB) (BD Biosciences) for 30 minutes at 4 °C. After staining, samples were washed once in ABB and finally suspended, and FACS acquired in ABB as reported earlier[55].

Transmission electron microscopy.

Variously activated $CD8^+$ T cells from pMel-1 mice were fixed with 4% glutaraldehyde solution and stained for electron microscopy. Fixed cells were post fixed in 1% osmium tetroxide (OsO_4) in PBS, rinsed in PBS then embedded in 2% agarose. The cells were then dehydrated through graded ethanol to propylene oxide and infiltrated with 1:1 propylene oxide:Embed 812 resin (Electron Microscopy Sciences) overnight, 1:3 propylene oxide:Embed 812 resin for 4 h and, finally, 100% Embed 812 resin overnight. The beam capsules were cured at 70 °C for 48 h before sectioning. Thin sections (90 nm) were cut with a Leica EM UC6 ultramicrotome (Leica Microsystems) on a diamond knife, placed onto a 300 mesh copper grid and stained using 2% uranyl acetate and Reynold's lead citrate. Samples were evaluated at 80 kV using a JEOL JM-1230 transmission electron microscope and images collected with an AMT 2K digital camera (Advanced Microscopy Techniques).

Metabolic assays.

For estimation of various metabolic characteristics, MEKi-treated $CD8^+$ T cells were activated with gp100 peptide with/without MEKi for 48 h, followed by mitochondrial stress tests (SeaHorse Bioscience), performed as per the manufacturer's specifications. OCR and ECAR were measured with an XFp flux analyzer (Seahorse Bioscience). For all assays, 160,000 cell per ml were plated onto culture plates using Cell-Tak (BD Biosciences). OCR and ECAR were measured in unbuffered DMEM (Agilent Biotechnologies) supplemented with 10 mM D-glucose (Sigma-Aldrich), 10 mM L-glutamine and 2.5 mM pyruvate, as indicated. SRC was calculated according to the previously published method[20]. The rates of FAO were determined in variously treated cells, as described above, using a Seahorse XF Palmitate-BSA FAO Reagent kit, used according to the manufacturer's instructions (Agilent Biotechnologies). In a few experiments, cells were activated in the presence of oligomycin (100 nM), to block mitochondrial respiration, or etomoxir (10 μg ml^{-1}), an inhibitor of FAO, followed by estimation of cell proliferation as an indicator of cellular activation, or Sca1 as an indicator of T_{SCM} generation.

Metabolomics and lipidomics.

We used multiple reaction monitoring mass spectrometry (MRM) for the quantification of 270 endogenous metabolites and 1,100 lipids using a triple quadrupole mass spectrometer operating in the MRM mode (QTRAP 5500 LC–MS/MS System, SCIEX). For this study, approximately 5 million cells were suspended in 20 μl of water:methanol:IPA (35:25:40) and the sample tube was plunged into dry ice for 30 s and a water bath at 37 °C for 90 s. Freeze-thaw cycles were repeated three times followed by sonication for 30 s. Metabolite extraction was performed by the addition of 120 μl of extraction buffer (methanol:water 50:50) containing 200 ng ml^{-1} of debrisoquine (DBQ) as internal standard for positive mode, and

200 ng ml^{-1} of 4-nitrobenzoic acid as internal standard for negative mode. The samples were vortexed for 30 s and incubated on ice for 20 min, followed by incubation at −20 °C for 20 min. Samples were centrifuged at 13,000 r.p.m. for 20 min at 4 °C. The supernatant was transferred to an MS vial for liquid chromatography–mass spectrometry (LC–MS) analysis. Five microliters of the prepared sample was injected onto a Kinetex 2.6 µm, 100 Å 100 mm × 2.1 mm column (Phenomenex) using an SIL-30 AC auto sampler (Shimadzu) connected with a high flow LC-30AD solvent delivery unit (Shimadzu) and CBM-20A communication bus module (Shimadzu) online with QTRAP 5500 (SCIEX) operating in electrospray positive- and negative-ion mode. A binary solvent gradient comprising of water with 0.1% formic acid (solvent A) and acetonitrile with 0.1% formic acid (solvent B) was used. The extracted metabolites were resolved at 0.2 ml min^{-1} flow rate starting with 100% of solvent A and held for 2.1 min and moving to 5% of solvent A over a time period of 12 min and held for 1 min, and equilibrating to initial conditions over a time period of 7 min using an auto sampler temperature of 15 °C and oven temperature of 30 °C. Source and gas settings for the method were as follow: curtain gas, 35; CAD gas, medium; ion spray voltage, 2,500 V in positive mode and −4,500 V in negative mode; temperature, 400 °C; nebulizing gas, 60; heater gas, 70. The data were normalized to internal standard area and processed using MultiQuant v.3.0.3 (SCIEX). To ensure high quality and reproducibility of LC–MS data, the column was initially conditioned using the pooled quality control samples. Subsequently, pooled quality control samples were injected periodically (after every five sample injections) to monitor any shifts in signal intensities and retention time, as measures of reproducibility and data quality for the LC–MS. We also used NIST plasma as a reference standard to monitor variance in instrument performance. Blank solvent was run between sets of samples to monitor any sample carryover.

We also analyzed a complex lipid panel that was designed to measure 19 classes of lipid molecules, which includes diacylglycerols (DAG), cholesterol esters (CE), sphingomyelins (SM), phosphatidylcholine (PC), triacylglycerols (TAG), free fatty acids (FFA), ceramides (CE), dihydroceramides (DCER), hexosylceramide (HCER), lactosylceramide (LCER), phosphatidylethanolamine (PE), lysophosphatidylcholine (LPC), lysophosphatidylethanolamine (LPE), phosphatidic acid (PA), lysophosphatidic acid (LPA), phosphatidylinositol (PI), lysophosphatidylinositol (LPI), phosphatidylglycerol (PG) and phosphatidylserine (PS) using a QTRAP 5500 LC–MS/MS System (SCIEX). For this purpose, approximately 5 million cells were suspended in 20 µl of water:methanol:IPA (35:25:40) and the sample tube was plunged into dry ice for 30 s and a water bath at 37 °C for 90 s. The freeze-thaw cycle was repeated three times and then samples were sonicated for 30 s. Chilled isopropanol (120 µl) containing internal standards was added and samples were vortexed. The samples were vortexed again for 1 min and kept on ice for 30 min. Samples were incubated at −20 °C for 2 h for complete protein precipitation. The samples were centrifuged at 13,000*g* for 20 min at 4 °C. The supernatant was transferred to the MS vial for LC–MS analysis. Five microliters of each sample was injected onto an XBridge amide column 3.5 µm, 4.6 mm × 100 mm (Waters Corporation) using a SIL-30 AC auto sampler (Shimadzu) connected with a high flow LC-30AD solvent delivery unit (Shimadzu) and CBM-20A communication bus module (Shimadzu) online with QTRAP 5500 (SCIEX) operating in positive- and negative-ion mode. A binary solvent comprising of

acetonitrile:water 95:5 with 10 mM ammonium acetate as solvent A and acetonitrile:water 50:50 with 10 mM ammonium acetate as solvent B was used for the resolution. Lipids were resolved at 0.7 ml min^{-1} flow rate, and initial gradient conditions started with 100% of solvent A, shifting towards 99.9% of solvent A over a time period of 3 min, 94% of solvent A over a time period of 3 min and 25% of solvent A over a period of 4 min. Finally, washing with 100% of solvent B for 6 min and equilibrating to initial conditions (100% of solvent A) over a time period of 6 min using an auto sampler temperature of 15 °C and an oven temperature of 35 °C. Source and gas settings were as follow: curtain gas, 30; CAD gas, medium; ion spray voltage, 5.5 kV in positive mode and −4.5 kV in negative mode; temperature, 550 °C; nebulizing gas, 50; heater gas, 60. The data were normalized to the respective internal standard area for each class of lipid and processed using MultiQuant v.3.0.3 (SCIEX). The quality and reproducibility of the LC–MS data were ensured using a number of measures. The column was conditioned using the pooled quality control samples. The pooled quality control sample was injected after every five sample injections to monitor the reproducibility and quality of the LC–MS data. We also used blank solvent runs between sets of samples to monitor carryover effects.

Cell proliferation assay.

To estimate the effect of various inhibitors on $CD8^+$ T cell proliferation, freshly isolated $CD8^+$ T cells were labeled with VCT as per the manufacturer's instructions. Labeled cells were activated with gp100 alone or in combination with other inhibitors, namely MEKi (1 μM; AZD6244), 2DG (2 μM; Sigma-Aldrich), oligomycin (100 nM; Sigma-Aldrich), etomoxir (10 μg ml^{-1}; Sigma-Aldrich), ERK1/2i (100 nM; SCH772984; Selleckchem), cyclin D1i (5 μM; arcyriaflavin A; Tocris Bioscience) and PGC1αi (5 μM; SR-18292; Sigma-Aldrich). After 48 h of cell activation, cells were collected and analyzed for progression of proliferation by looking at the VCT dilution estimated by FACS analysis.

siRNA for MEK1 and MEK2.

For knockdown of MEK1/2, pMel $CD8^+$ T cells were incubated with MEK1 and MEK2 siRNA (1 μM; Dharmacon) in 1% FBS medium overnight. Next day, medium containing gp100 (1 μM) was added to the wells for cell activation. Cells were collected after 48 h of incubation at 37°C. The knockdown of MEK1/2 was estimated by FACS analysis of the treated cells using appropriately conjugated anti-MEK1 and anti-MEK2.

Quantitative PCR with reverse transcription analysis.

Total RNA was extracted from gp100 or gp100 plus MEKi-activated $CD8^+$ T cells using TRIzol reagent (Invitrogen), and dissolved in RNase-free water. One μg total RNA was subjected to single-strand complementary DNA synthesis using iScript cDNA Synthesis Kit (Bio-Rad). Expression of *Slc2a1* (F-GGATCCCAGCAGCAAGAAGGT; R-CGTAGCGGTGGTTCCATGTT), *Cpt1a* (F-GGACTCCGCTCGCTCATT; R-GAGATCGATGCCATCAGGGG), *Ifng* (F-ACTGGCAAAAGGATGGTGACA; R-TGGACCTGTGGGTTGTTGAC), *Gzmb* (F-GACAAAGGCAGGGGAGATCAT; R-CGAATAAGGAAGCCCCCACA), *Prf1* (TTGGTGGGACTTCAGCTTTCC; R-CCATACACCTGGCACGAACT), *Eomes* (F-AAACACGGATATCACCCAGC; R-GGGCTTGAGGCAAAGTGTTG), *Klf2* (F-

GCGTACACACACAGGTGAGA; R-GCACAAGTGGCACTGAAAGG) was analyzed. Mitochondrial DNA (mtDNA) and total nuclear DNA (nDNA) were estimated using the primers and conditions reported earlier[56]. Data were procured using StepOnePlus Real-Time PCR System from Applied Biosystems and normalized to the geometric mean of the housekeeping gene *Actb* (β-actin).

Western blot.

FACS-sorted human $CD8^+$ T cells were activated as described above. Cell lysates (RIPA buffer + 1% phosphatase inhibitor + 1% protease inhibitor) of pMel-1 $CD8^+$ T cells were prepared following various treatments. Protein concentrations in cell lysates were determined by Pierce BCA Protein Assay Kit (ThermoFisher Scientific). Protein (30–40 μg) was loaded onto Novex 4–12% Tris-Glycin Mini Gels (ThermoFisher Scientific) followed by transfer onto nitrocellulose membranes. Membranes were blocked with 3% BSA in Tris buffer followed by overnight probing with antibodies against p-mTORC1 and total mTORC1 by western blot. The blots were developed with appropriate (anti-rabbit or anti-mouse) HRP-conjugated secondary antibodies. The level of β-actin was used as a control. Densitometric analysis of the bands was performed using a software (Image Studio Lite v.5.0) from LI-COR (https://www.licor.com/bio/image-studio-lite/).

Statistical analysis.

Sample sizes were determined by prior experience and to achieve a confidence level of at least 95%. All summary statistics (average values, s.d., s.e.m., significant differences between groups) were calculated using GraphPad Prism v.6.0 or Excel, as appropriate. Statistical significance between groups was determined by unpaired, one-tailed Student's *t*-test or one-way analysis of variance (ANOVA) ($P \leq 0.05$ was considered statistically significant). Survival in various groups was compared with GraphPad Prism using log-rank (Mantel–Cox) test.

SK plots were generated by internally developed software (https://skylineplotter.shinyapps.io/SkyLinePlotter/). Contrary to the survival plot generated using GraphPad Prism, the SK plot gives dynamic simultaneous presentation of tumor volumes and mouse survival at a specific time point.

Statistical analyses of mass spectrometry data.

The raw LC–MS data were initially normalized by internal standards. The preprocessing was followed up by quality control procedures which involve the calculation of the normalized intensities based on relative standard deviation for each feature. The features with more than 15% coefficient of variation were filtered out. The features with missing value of more than 20% were also filtered out, and, for less than 20% of missing value, those features were imputed by half of the minimum positive value in the original data. The remaining high-quality peak intensities were then QC-RLSC[57] normalized and summarized for quantification. The *P* values for binary comparisons were calculated by two-tailed unpaired Student's *t*-test, whereas *P* values of less than 0.05 exclusively were considered significant. Furthermore, *P* values were corrected for multiple testing using the Benjamini–

Hochberg procedure, which limits the false discovery rates. PCA, hierarchical clustering and all statistical analyses were performed using R (v.4.0.1).

Reporting Summary.

Further information on research design is available in the Nature Research Reporting Summary linked to this article.

Extended Data

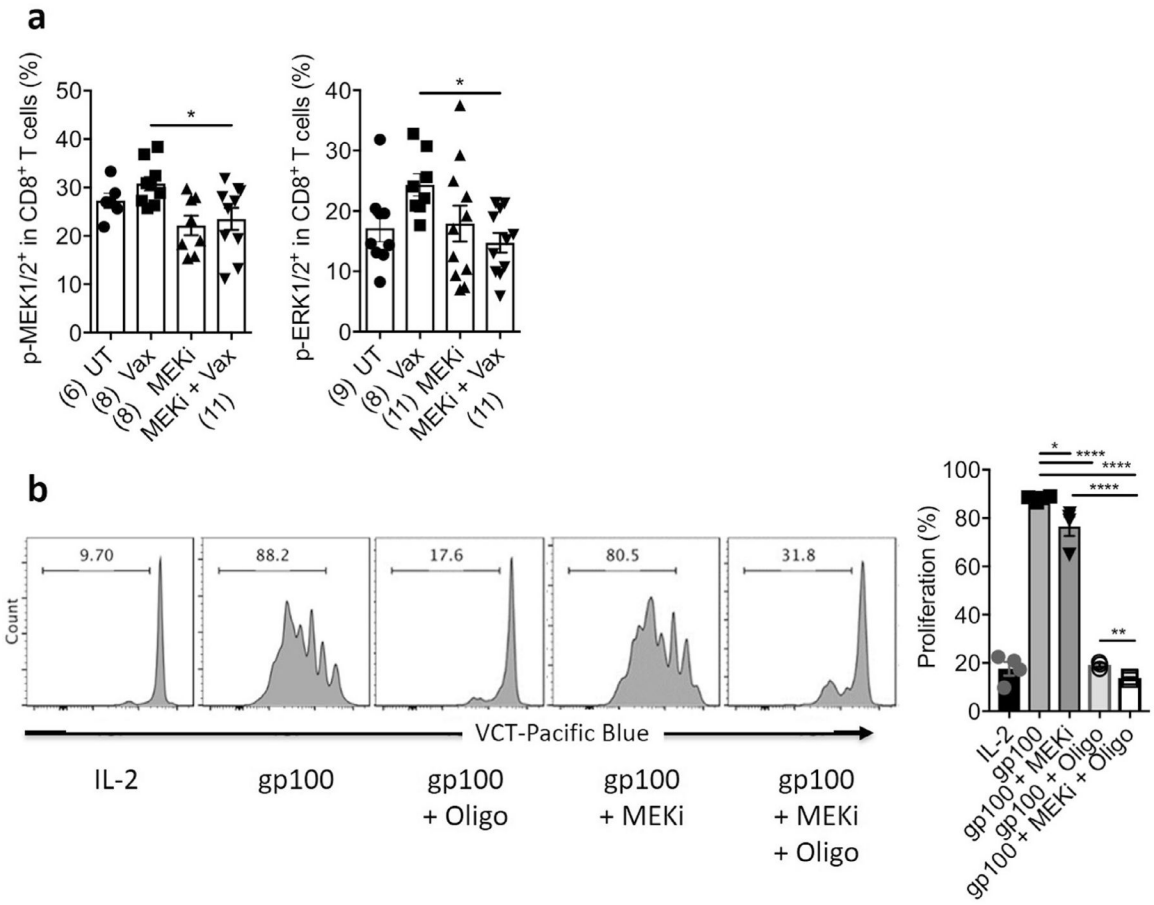

Extended Data Fig. 1 |. MEKi enhances mitochondrial respiration in CD8+ T cells.
Related to Figs. 1 and 2. a, Frequencies of phosphorylated-(p)-MEK1/2 and ERK1/2 $CD8^+$ T cells in the TME as estimated by FACS analysis. Representative data from one of two experiments are shown. Each symbol corresponds to one mouse with the indicated number of mice per group given in parentheses. The error bars indicate the s.e.m. Statistical analysis was performed by unpaired, one-tailed Student's t-test (*P≤0.05). **b**, Determination of effect of inhibition of mitochondrial respiration by oligomycin on proliferation (by VCT dilution) of gp100-activated and MEKi-treated $CD8^+$ T cells. Representative results from one of two experiments performed in triplicates are shown. The error bars indicate the s.e.m. Statistical analysis was performed by unpaired, one-tailed Student's t-test (*P≤0.05; **P≤0.01; ****P≤0.0001).

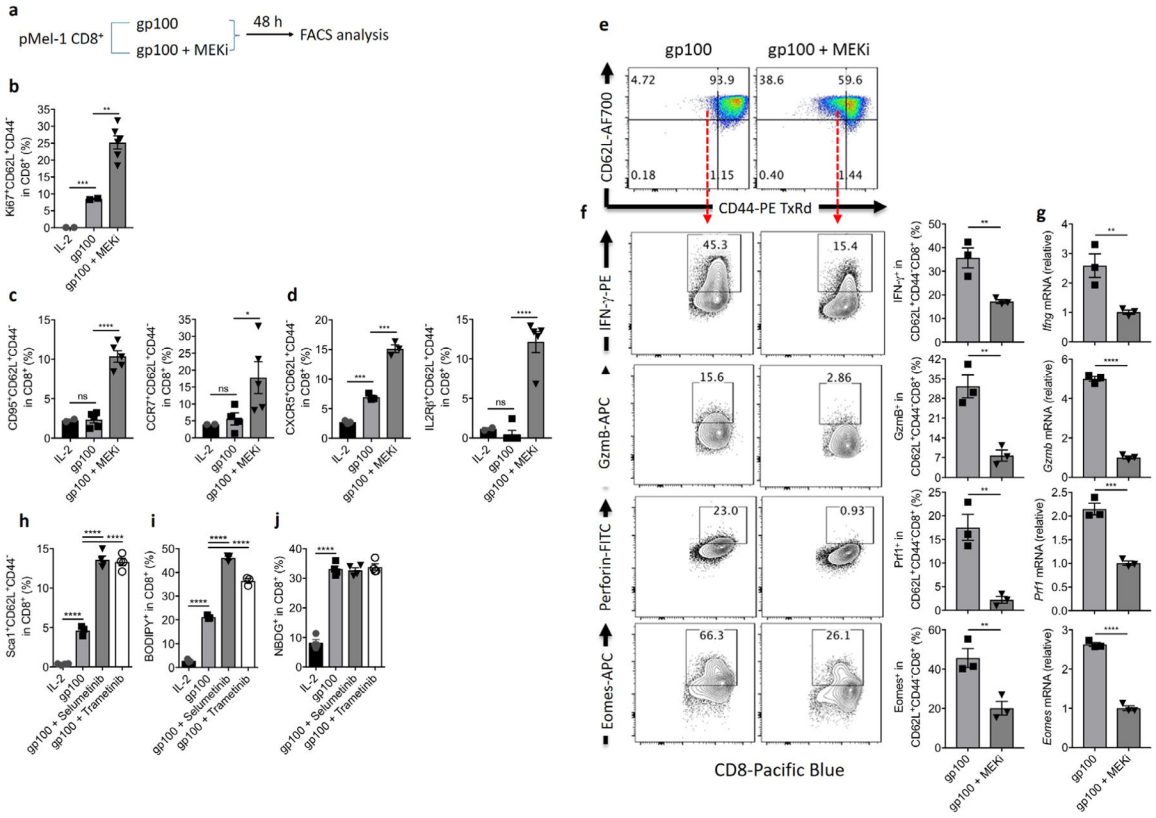

Extended Data Fig. 2 |. Expression profiles for markers of proliferation, memory, activation, apoptosis, effector functions and exhaustion on in vitro MEKi-treated pMel-1 CD8+ T cells and effects of MEKi, trametinib on TSCM induction and cellular metabolism.

Related to Figs. 4 and 6. a–**d**, Scheme of pMel-1 $CD8^+$ T cell activation and analysis (**a**); FACS analysis of $Ki67^+$ (**b**); $CD95^+$ and $CCR7^+$ (**c**); $CXCR5^+$ and $IL2R\beta^+$ (**d**) in $CD62L^+CD44^-$ $CD8^+$ T cells after various treatments as shown in figures. Representative results from one of two experiments performed in triplicates are shown. The error bars indicate the s.e.m. Statistical analysis was performed by unpaired, one-tailed Student's t-test (*P≤0.05; **P≤0.01; ***P≤0.001; ****P≤0.0001; ns: non-significant). **e**–**g**, FACS micrographs showing the cell phenotype in the naive compartment ($CD62L^+CD44^-$) after 48 h activation under various conditions as shown in picture (**e**); FACS analysis of expression of IFN-γ, Granzyme B, Perforin, KLRG1 and Eomes on $CD62L^+CD44^-$ cells in the naïve cell compartment (marked by dotted red arrows) (**f**); Expression levels of mRNA of various effector and exhaustion markers relative to *Actb* after *in vitro* activation of pMel-1 $CD8^+$ T cells with gp100 with/without MEKi (**g**). Experiments were repeated twice with similar results and representative results from one experiment are shown. The error bars indicate the s.e.m. Statistical analysis was performed by unpaired, one-tailed Student's t-test (**P≤0.01; ***P≤0.001; ****P≤0.0001). **h**–**j**, Comparative analysis of induction of T_{SCM} cells (**h**); Estimation of FA (**i**) and glucose (**j**) uptake in $CD8^+$ T cells that were activated in the presence of selumetinib or trametinib. Representative results from one of two experiments performed in triplicates are shown. The error bars indicate the s.e.m. Statistical analysis was performed by unpaired, one-tailed Student's t-test (****P≤0.0001).

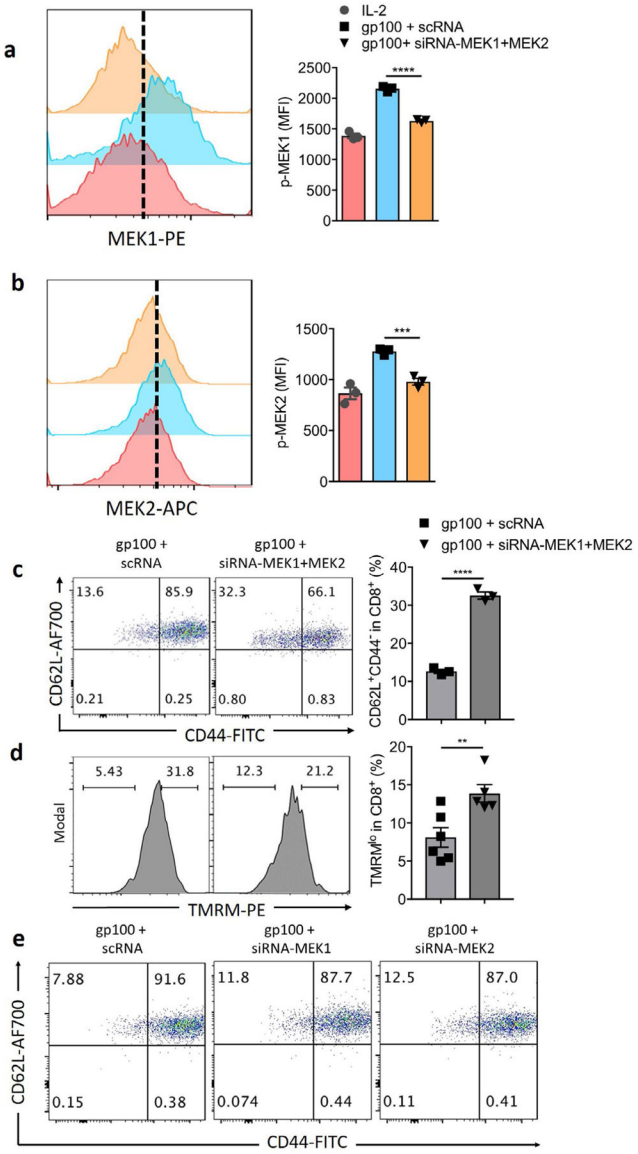

Extended Data Fig. 3 |. In vitro analysis of effect of MEK1 and MEK2 knock down (MEK1/2KD) using siRNA on generation of naive and TSCM cells.

Related to Fig. 4. a, b, Confirmation of knock down of MEK1 (**a**) and MEK2 (**b**) by FACS analysis after siRNA treatment. Data are representative of two experiments performed in triplicates. The error bars indicate the s.e.m. Statistical analysis was performed by unpaired, one-tailed Student's t-test (***P≤0.001; ****P≤0.0001). **c**, **d**, Relative frequencies of $CD62L^{+}CD44^{-}$ cells (**c**) and mitochondrial potential (TMRM) (**d**) of $CD8^{+}$ T cells in which MEK1/2 was knocked down. Data are representative of three experiments performed in triplicate. The error bars indicate the s.e.m. Statistical analysis was performed by unpaired, one-tailed Student's t-test (**P≤0.01; ****P≤0.0001) **e**, Memory phenotypes generated after MEK1KD or MEK2KD in pMel-1 $CD8^{+}$ T cells. Data are representative of two experiments performed in triplicates.

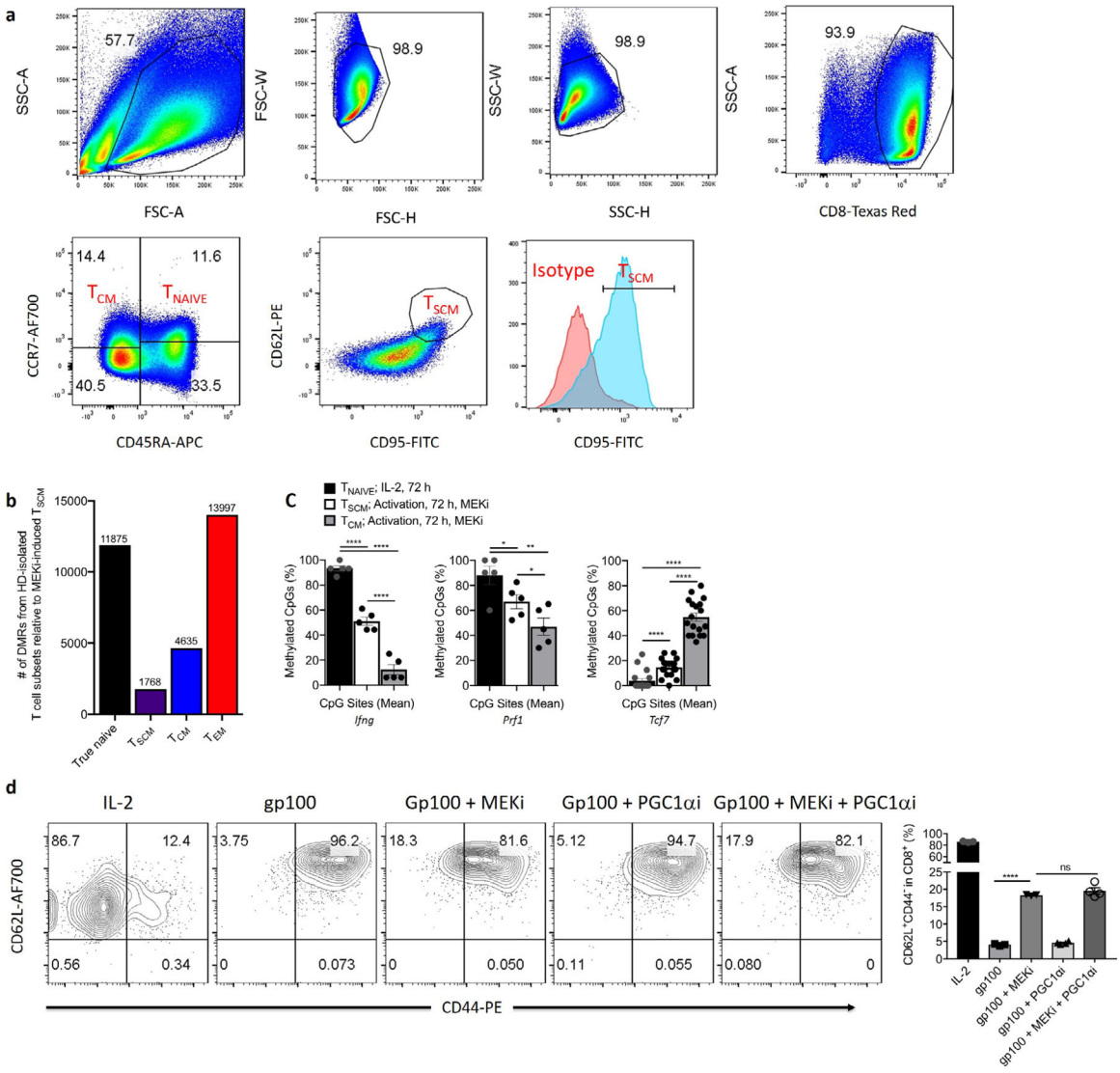

Extended Data Fig. 4 |. Gating strategy and methylation status of MEKi-treated CD8+ T cells. Related to Figs. 5 and 7. a, Gating strategy for generation of T_{SCM} cells from human $CD8^+$ T cells. **b**, A graphical representation of the number of DMRs among the MEKi T_{SCM} (one WGBS sample) versus freshly isolated naive, bonafide T_{SCM}, T_{CM}, and T_{EM} (one WGBS sample for each) from healthy donors (HD). **c**, Statistical analysis of the methylation status of human T_{NAIVE}, T_{SCM} and T_{CM} cells at *Ifng*, *Prf1* and *Tcf7* gene loci, as noted in the figure (related to Fig. 5e–g). Representative data from one of two experiments is shown. The error bars indicate the s.e.m. Statistical analysis was performed by unpaired, one-tailed Student's t-test (*P≤0.05; **P≤0.01; ****P≤0.0001). **d**, Estimation of CD62L and CD44 on pMel-1 CD8 cells after activation under various conditions as listed in the figure. Representative results from one of three experiments performed in triplicates are shown. The error bars indicate the s.e.m. Statistical analysis was performed by unpaired, one-tailed Student's t-test (****P≤0.0001; ns: non-significant).

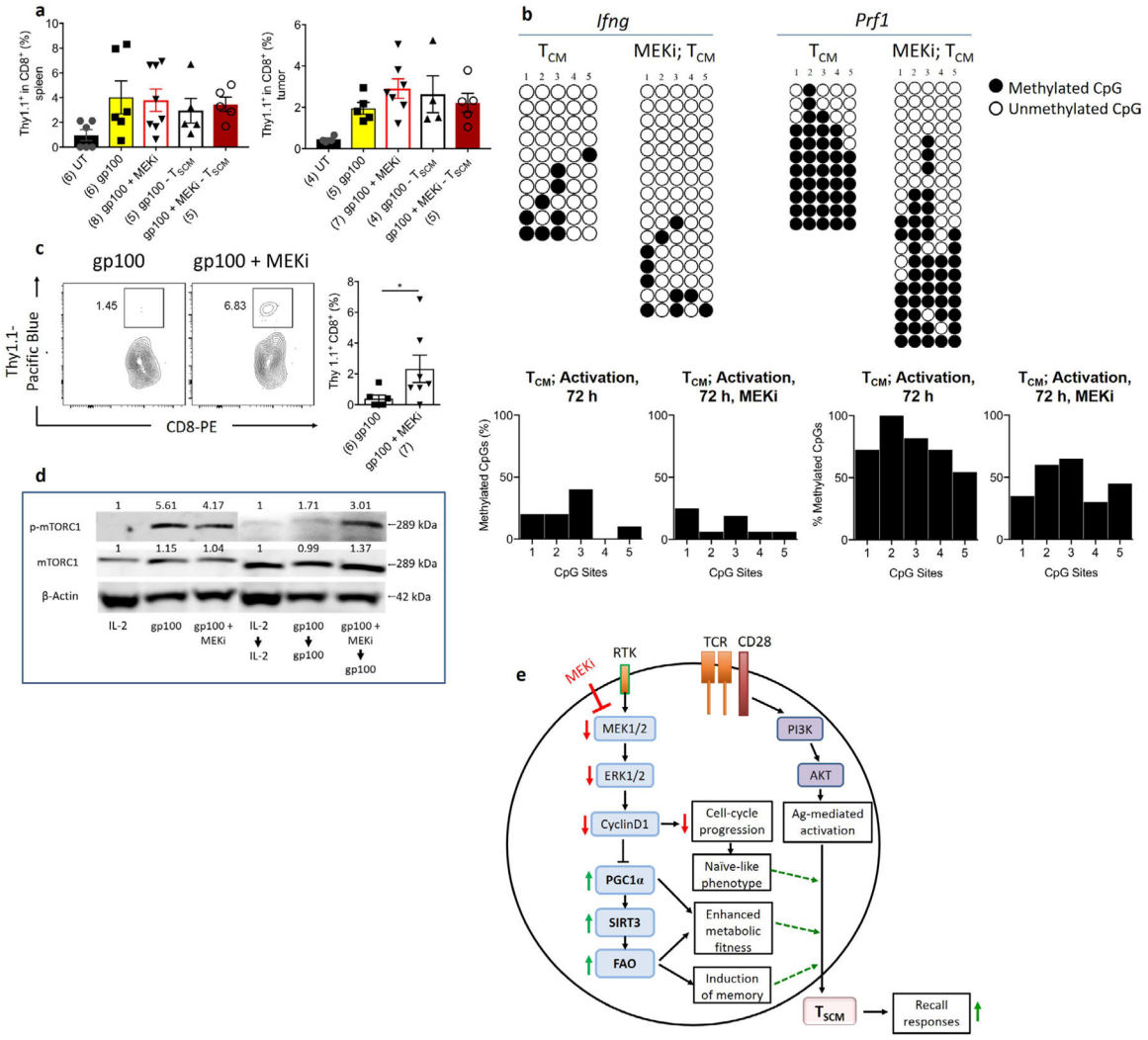

Extended Data Fig. 5 |. Frequency of CD8+ T cells in various tissues following ACT, the expression levels of mTORC1 in MEKi-treated CD8+ T cells, and a proposed model for MEKi-mediated TSCM generation.

Related to Fig. 8. a, The frequency of $CD8^+$ T cell engrafted in spleen and tumors of mice that received variously treated pMel-1 $CD8^+$ T cells (48 h post-T cell infusion). FACS analysis of the tumor and spleen samples was performed by gating upon Thy1.1 cell population. A representative of two experiments is shown. Each symbol corresponds to one mouse with the indicated number of mice per group given in parentheses. The error bars indicate the s.e.m. Statistical analysis was performed by unpaired, one-tailed Student's t-test. Significant differences in engraftment were not observed between MEKi-treated and untreated spleen and tumor samples. **b**, Loci-specific bisulfite sequencing analysis of the *Ifng* and *Prf1* in T_{CM} $CD8^+$ T cells generated after activation of human $CD8^+$ T cells with anti-CD3/28 with or without MEKi treatment. Horizontal lines represent individual sequenced clones from the pool of FACS-purified $CD8^+$ T cells. Bar graphs represent the frequencies of methylated CpGs in respective sample as shown in the figure. Representative data from one of two experiments are shown. **c**, Estimation of numbers of adoptively transferred cells in tumors of variously treated mice. The mice were sacrificed at 22

days after ACT and tumors were harvested. Samples were stained and processed for FACS analysis. A representative of two experiments is shown. Each symbol represents one mouse with the indicated number of mice per group given in parentheses. The error bars indicate the s.e.m. Statistical analysis was performed by unpaired, one-tailed Student's t-test (*P≤0.05). **d**, Levels of phosphorylated-(p)-mTORC1 and total mTORC1 in MEKi-treated mouse $CD8^+$ T cells during initial cell activation and following antigenic re-challenge as detailed in the figure. Expression of β-actin is shown as a control. Number on the bands show band intensity. Experiments were repeated twice with similar results. **e**, Proposed model for MEKi-mediated T_{SCM} generation. Inhibition of MEK1/2 during antigen-activation of naive cells: 1) results in a decrease in the levels of ERK1/2 and cyclin D1, delaying cell division and accumulating these cells in early phases of differentiation; 2) results in an increase in PGC1α and its downstream SIRT3, enhancing FAO-mediated metabolic fitness that drives memory generation; and 3) does not affect PI3K-Akt-mediated T cell activation. This crosstalk between MAPK pathway, cellular metabolism and TCR-mediated signaling after MEK-inhibition leads to induction of memory characteristics in naive $CD8^+$ T cells, generating T_{SCM}. These T_{SCM} produce highly activated effector cells following re-stimulation with the cognate antigen resulting in robust recall responses.

Acknowledgements

We are grateful to Jeannie and Tony Loop for their generous support to SNK's laboratory. We acknowledge the Georgia Cancer Center, Augusta University internal support grant to S.N.K. and Flow Cytometry Core Facility at Lombardi Comprehensive Cancer Center. We acknowledge the Metabolomics and Flow Cytometry/Cell Sorting Shared Resource in Georgetown University, which is partially supported by NIH/NCI/CCSG grant P30-CA051008 and NIH S10 grant S10OD016213. We thank S. Bansal for technical assistance with LC–MS data acquisition and S. Li for LC–MS data processing and analysis. This study was supported in part by NIH grant 1 R01 CA237311 01A1 to B.Y. and NIH grants R01-CA184185, R01-CA233512 and P30-CA076292 and The Florida Department of Health grant no. 20B04 to P.C.R. We acknowledge the contribution of P. Finger from the electron microscopy service at the Jackson Laboratory for assistance with electron microscopy.

Data availability

For healthy adult donors, PBMCs were collected through the St. Jude's Blood Bank; samples for WGBS were collected under institutional review board protocol no. XPD15–086 as published earlier[32]. In vitro, in vivo and flow cytometry data are included in this published article and its Extended Data Figures. All other relevant data are available from the corresponding author upon reasonable request. Source data are provided with this paper.

References

1. Lim WA & June CH The principles of engineering immune cells to treat cancer. Cell 168, 724–740 (2017). [PubMed: 28187291]
2. Jones PA, Issa JP & Baylin S Targeting the cancer epigenome for therapy. Nat. Rev. Genet 17, 630–641 (2016). [PubMed: 27629931]
3. Sierra JR, Cepero V & Giordano S Molecular mechanisms of acquired resistance to tyrosine kinase targeted therapy. Mol. Cancer 9, 75 (2010). [PubMed: 20385023]
4. Carr EL et al. Glutamine uptake and metabolism are coordinately regulated by ERK/MAPK during T lymphocyte activation. J. Immunol 185, 1037–1044 (2010). [PubMed: 20554958]
5. Terada Y et al. Regulation of cyclin D1 expression and cell cycle progression by mitogen-activated protein kinase cascade. Kidney Int 56, 1258–1261 (1999). [PubMed: 10504469]

6. Pearce EL, Poffenberger MC, Chang CH & Jones RG Fueling immunity: insights into metabolism and lymphocyte function. Science 342, 1242454 (2013). [PubMed: 24115444]
7. Scharping NE et al. The tumor microenvironment represses T cell mitochondrial biogenesis to drive intratumoral T cell metabolic insufficiency and dysfunction. Immunity 45, 701–703 (2016). [PubMed: 27653602]
8. Liu L et al. The BRAF and MEK inhibitors dabrafenib and trametinib: effects on immune function and in combination with immunomodulatory antibodies targeting PD-1, PD-L1, and CTLA-4. Clin. Cancer Res 21, 1639–1651 (2015). [PubMed: 25589619]
9. Ebert PJR et al. MAP kinase inhibition promotes T cell and anti-tumor activity in combination with PD-L1 checkpoint blockade. Immunity 44, 609–621 (2016). [PubMed: 26944201]
10. Hu-Lieskovan S et al. Improved antitumor activity of immunotherapy with BRAF and MEK inhibitors in BRAF(V600E) melanoma. Sci. Transl. Med 7, 279ra41 (2015).
11. McCubrey JA et al. Mutations and deregulation of Ras/Raf/MEK/ERK and PI3K/PTEN/Akt/mTOR cascades which alter therapy response. Oncotarget 3, 954–987 (2012). [PubMed: 23006971]
12. Kono M et al. Role of the mitogen-activated protein kinase signaling pathway in the regulation of human melanocytic antigen expression. Mol. Cancer Res 4, 779–792 (2006). [PubMed: 17050671]
13. Gattinoni L, Speiser DE, Lichterfeld M & Bonini C T memory stem cells in health and disease. Nat. Med 23, 18–27 (2017). [PubMed: 28060797]
14. Abdelsamed HA et al. Human memory CD8 T cell effector potential is epigenetically preserved during in vivo homeostasis. J. Exp. Med 214, 1593–1606 (2017). [PubMed: 28490440]
15. Troiani T et al. Intrinsic resistance to selumetinib, a selective inhibitor of MEK1/2, by cAMP-dependent protein kinase A activation in human lung and colorectal cancer cells. Br. J. Cancer 106, 1648–1659 (2012). [PubMed: 22569000]
16. Hong JJ, Amancha PK, Rogers K, Ansari AA & Villinger F Re-evaluation of PD-1 expression by T cells as a marker for immune exhaustion during SIV infection. PLoS ONE 8, e60186 (2013). [PubMed: 23555918]
17. Wherry EJ T cell exhaustion. Nat. Immunol 12, 492–499 (2011). [PubMed: 21739672]
18. Traves PG et al. Relevance of the MEK/ERK signaling pathway in the metabolism of activated macrophages: a metabolomic approach. J. Immunol 188, 1402–1410 (2012). [PubMed: 22190182]
19. Field CS et al. Mitochondrial integrity regulated by lipid metabolism is a cell-intrinsic checkpoint for Treg suppressive function. Cell Metab 31, 422–437.e5 (2020). [PubMed: 31883840]
20. van der Windt GJ et al. Mitochondrial respiratory capacity is a critical regulator of $CD8^+$ T cell memory development. Immunity 36, 68–78 (2012). [PubMed: 22206904]
21. Ibitokou SA et al. Early inhibition of fatty acid synthesis reduces generation of memory precursor effector T cells in chronic infection. J. Immunol 200, 643–656 (2018). [PubMed: 29237780]
22. Bhalla K et al. Cyclin D1 represses gluconeogenesis via inhibition of the transcriptional coactivator PGC1α. Diabetes 63, 3266–3278 (2014). [PubMed: 24947365]
23. Duronio RJ & Xiong Y Signaling pathways that control cell proliferation. Cold Spring Harb. Perspect. Biol 5, a008904 (2013). [PubMed: 23457258]
24. Lee Y et al. Cyclin D1–Cdk4 controls glucose metabolism independently of cell cycle progression. Nature 510, 547–551 (2014). [PubMed: 24870244]
25. Kong X et al. Sirtuin 3, a new target of PGC-1α, plays an important role in the suppression of ROS and mitochondrial biogenesis. PLoS ONE 5, e11707 (2010). [PubMed: 20661474]
26. Martin MD & Badovinac VP Defining memory CD8 T cell. Front. Immunol 9, 2692 (2018). [PubMed: 30515169]
27. Herndler-Brandstetter D et al. $KLRG1^+$ effector $CD8^+$ T cells lose KLRG1, differentiate into all memory T cell lineages, and convey enhanced protective immunity. Immunity 48, 716–729.e8 (2018). [PubMed: 29625895]
28. Gattinoni L et al. A human memory T cell subset with stem cell–like properties. Nat. Med 17, 1290–1297 (2011). [PubMed: 21926977]
29. Rosenblum MD, Way SS & Abbas AK Regulatory T cell memory. Nat. Rev. Immunol 16, 90–101 (2016). [PubMed: 26688349]

30. Sukumar M et al. Mitochondrial membrane potential identifies cells with enhanced stemness for cellular therapy. Cell Metab 23, 63–76 (2016). [PubMed: 26674251]
31. Carlson CM et al. Kruppel-like factor 2 regulates thymocyte and T-cell migration. Nature 442, 299–302 (2006). [PubMed: 16855590]
32. Abdelsamed HA et al. Beta cell-specific $CD8^+$ T cells maintain stem cell memory-associated epigenetic programs during type 1 diabetes. Nat. Immunol 21, 578–587 (2020). [PubMed: 32231298]
33. Pearce EL et al. Enhancing CD8 T-cell memory by modulating fatty acid metabolism. Nature 460, 103–107 (2009). [PubMed: 19494812]
34. Schumann J, Stanko K, Schliesser U, Appelt C & Sawitzki B Differences in CD44 surface expression levels and function discriminates IL-17 and IFN-γ producing helper T cells. PLoS ONE 10, e0132479 (2015). [PubMed: 26172046]
35. Araki K et al. mTOR regulates memory CD8 T-cell differentiation. Nature 460, 108–112 (2009). [PubMed: 19543266]
36. Jones RG & Pearce EJ MenTORing immunity: mTOR signaling in the development and function of tissue-resident immune cells. Immunity 46, 730–742 (2017). [PubMed: 28514674]
37. Pollizzi KN et al. mTORC1 and mTORC2 selectively regulate $CD8^+$ T cell differentiation. J. Clin. Invest 125, 2090–2108 (2015). [PubMed: 25893604]
38. Ruby CE, Redmond WL, Haley D & Weinberg AD Anti-OX40 stimulation in vivo enhances $CD8^+$ memory T cell survival and significantly increases recall responses. Eur. J. Immunol 37, 157–166 (2007). [PubMed: 17183611]
39. Fuertes Marraco SA et al. Long-lasting stem cell–like memory $CD8^+$ T cells with a naive-like profile upon yellow fever vaccination. Sci. Transl. Med 7, 282ra48 (2015).
40. Ahmed R et al. Human stem cell-like memory T cells are maintained in a state of dynamic flux. Cell Rep 17, 2811–2818 (2016). [PubMed: 27974195]
41. Whittaker E, Nicol MP, Zar HJ, Tena-Coki NG & Kampmann B Age-related waning of immune responses to BCG in healthy children supports the need for a booster dose of BCG in TB endemic countries. Sci. Rep 8, 15309 (2018). [PubMed: 30333506]
42. Thompson ED, Enriquez HL, Fu YX & Engelhard VH Tumor masses support naive T cell infiltration, activation, and differentiation into effectors. J. Exp. Med 207, 1791–1804 (2010). [PubMed: 20660615]
43. Li H et al. Dysfunctional CD8 T cells form a proliferative, dynamically regulated compartment within human melanoma. Cell 176, 775–789.e18 (2018). [PubMed: 30595452]
44. Fonseca R et al. Developmental plasticity allows outside-in immune responses by resident memory T cells. Nat. Immunol 21, 412–421 (2020). [PubMed: 32066954]
45. Kretschmer L et al. Differential expansion of T central memory precursor and effector subsets is regulated by division speed. Nat. Commun 11, 113 (2020). [PubMed: 31913278]
46. Verma V et al. PD-1 blockade in subprimed CD8 cells induces dysfunctional $PD\text{-}1^+CD38^{hi}$ cells and anti-PD-1 resistance. Nat. Immunol 20, 1231–1243 (2019). [PubMed: 31358999]
47. Gattinoni L et al. Wnt signaling arrests effector T cell differentiation and generates $CD8^+$ memory stem cells. Nat. Med 15, 808–813 (2009). [PubMed: 19525962]
48. Im SJ et al. Defining $CD8^+$ T cells that provide the proliferative burst after PD-1 therapy. Nature 537, 417–421 (2016). [PubMed: 27501248]
49. Jung YW, Kim HG, Perry CJ & Kaech SM CCR7 expression alters memory CD8 T-cell homeostasis by regulating occupancy in IL-7- and IL-15-dependent niches. Proc. Natl Acad. Sci. USA 113, 8278–8283 (2016). [PubMed: 27385825]
50. Ji Y et al. Identification of the genomic insertion site of Pmel-1 TCR α and β transgenes by next-generation sequencing. PLoS ONE 9, e96650 (2014). [PubMed: 24827921]
51. Lin KY et al. Treatment of established tumors with a novel vaccine that enhances major histocompatibility class II presentation of tumor antigen. Cancer Res 56, 21–26 (1996). [PubMed: 8548765]

52. Overwijk WW et al. gp100/pmel 17 is a murine tumor rejection antigen: induction of “self ”-reactive, tumoricidal T cells using high-affinity, altered peptide ligand. J. Exp. Med 188, 277–286 (1998). [PubMed: 9670040]

53. Xi Y & Li W BSMAP: whole genome bisulfite sequence MAPping program. BMC Bioinformatics 10, 232 (2009). [PubMed: 19635165]

54. Wu H et al. Detection of differentially methylated regions from whole-genome bisulfite sequencing data without replicates. Nucleic Acids Res 43, e141 (2015). [PubMed: 26184873]

55. Shrimali RK et al. Concurrent PD-1 blockade negates the effects of OX40 agonist antibody in combination immunotherapy through inducing T-cell apoptosis. Cancer Immunol. Res 5, 755–766 (2017). [PubMed: 28848055]

56. Guo W, Jiang L, Bhasin S, Khan SM & Swerdlow RH DNA extraction procedures meaningfully influence qPCR-based mtDNA copy number determination. Mitochondrion 9, 261–265 (2009). [PubMed: 19324101]

57. Rusilowicz M, Dickinson M, Charlton A, O’Keefe S & Wilson J A batch correction method for liquid chromatography–mass spectrometry data that does not depend on quality control samples. Metabolomics 12, 56 (2016). [PubMed: 27069441]

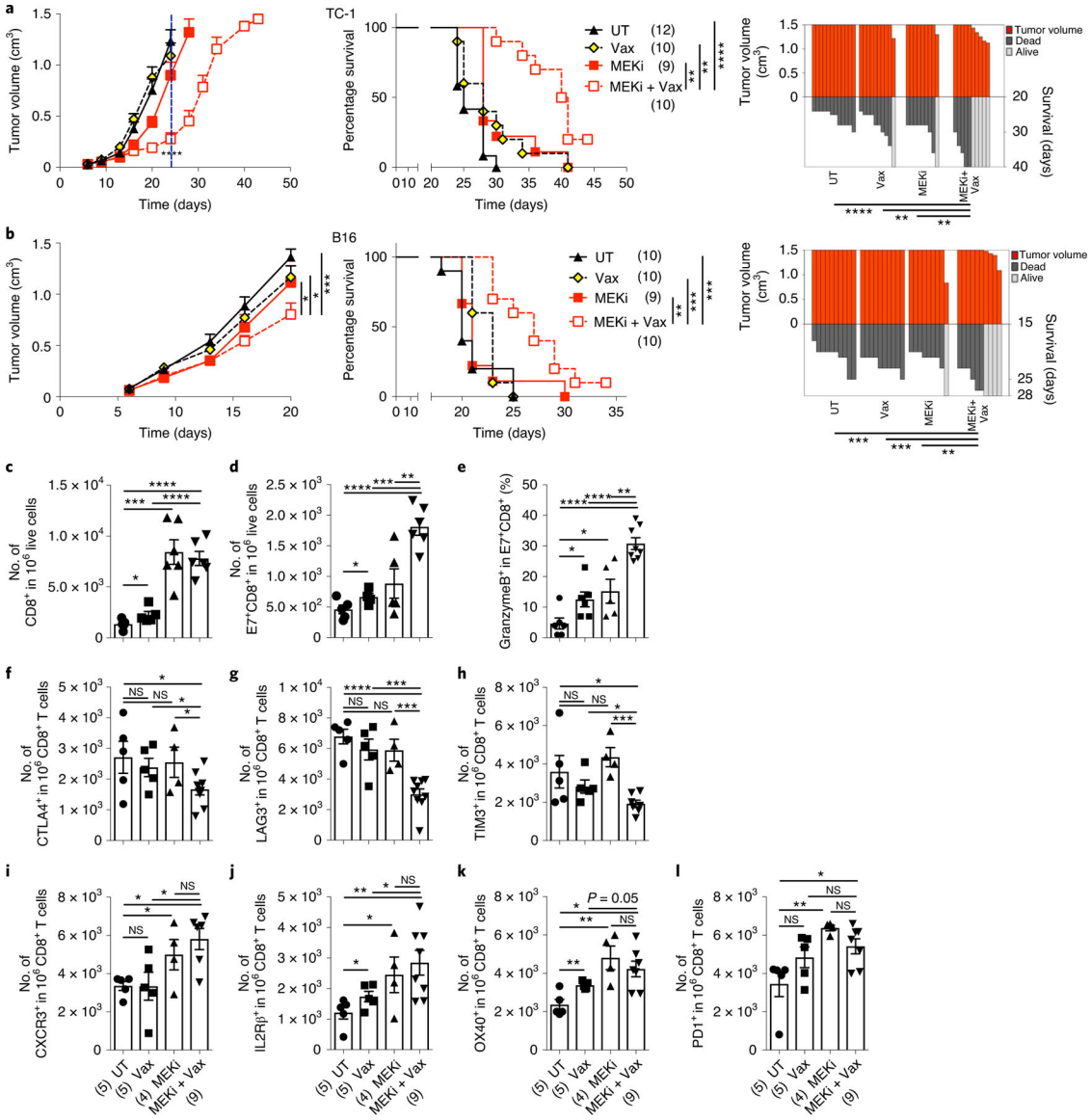

Fig. 1 |. MEKi supports the expansion of activated effector T cells in the TME leading to reduced tumor growth. a,b,

Tumor growth rate, mouse survival and SK plots in TC-1 (**a**) and B16F10 (**b**) tumor models after various treatments. Tumor growth and survival data are the average of two independent experiments with the indicated numbers of mice per group given in parentheses. The error bars indicate the s.e.m. For tumor growth, statistical analysis was performed by unpaired, one-tailed Student's *t*-test. The *P* value in the tumor growth graph in **a** is between Vax and MEKi plus Vax (****$P \leq 0.0001$) and for **b**, *$P \leq 0.05$, ***$P \leq 0.001$. Survival in various groups was compared using log-rank (Mantel–Cox) tests, **$P \leq 0.01$, ***$P \leq 0.001$, ****$P \leq 0.0001$ (**a**,**b**). UT, untreated. **c**–**l**, Analysis of immune infiltrate in tumors 2–3 days after second vaccination. Number of $CD8^+$ (**c**), $E7^+CD8^+$ T cells (**d**) and granzyme B^+ in $E7^+CD8^+$ T cells (**e**) in the TC-1 TME of variously treated mice. Number of $CTLA4^+$ (**f**), $LAG3^+$ (**g**), $TIM3^+$ (**h**), $CXCR3^+$ (**i**), IL-2Rβ$^+$ (**j**), $OX40^+$ (**k**), and PD-1^+ (**l**) $CD8^+$ T cells in the TME of variously treated mice as shown in the figure. Representative data from one

of two experiments are shown. Each symbol corresponds to one mouse with the indicated number of mice per group given in parentheses. The error bars indicate the s.e.m. Statistical analysis was performed by unpaired, one-tailed Student's *t*-test. *$P \leq 0.05$; **$P \leq 0.01$; ***$P \leq 0.001$; ****$P \leq 0.0001$; NS, not significant. See also Extended Data Fig. 1a.

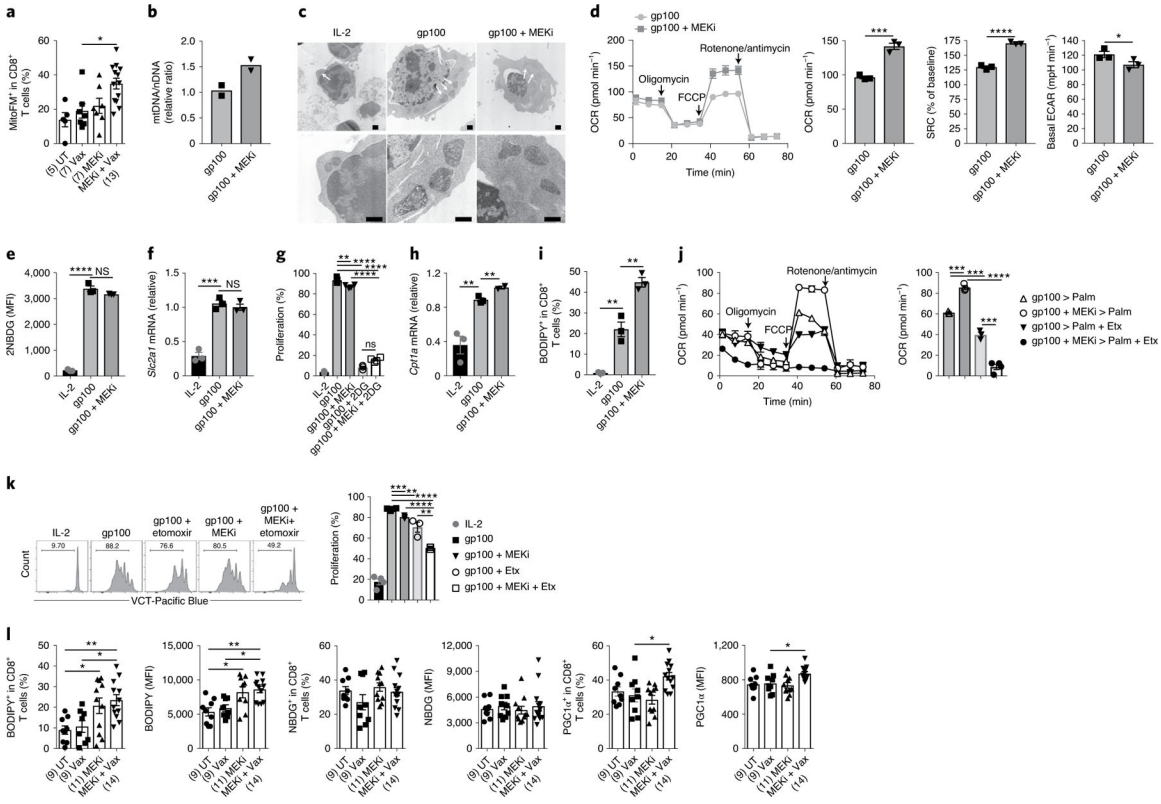

Fig. 2 |. MEKi-treated CD8+ T cells have enhanced mitochondrial respiration fueled by FAO. a, Mitochondrial mass in $CD8^+$ T cells after MEKi treatment of TC-1 tumor-bearing vaccinated animals in comparison to control animals. Representative results from one of the two experiments are shown. Each symbol corresponds to one mouse with the indicated number of mice per group given in parentheses. The error bars indicate the s.e.m. Statistical analysis was performed by unpaired, one-tailed Student's *t*-test (*$P \leq 0.05$). **b**, mtDNA/nDNA ratio in pMel-1 $CD8^+$ T cells activated with cognate gp100 peptide, with or without MEKi treatment. **c**, Transmission electron microscopic (TEM) analysis of mitochondrial morphology in variously treated $CD8^+$ T cells as shown in the figure. White arrows in the upper panels show the position of mitochondria in respective higher magnification in the lower panels. The scale bar in each micrograph is equivalent to 500 nm. Variously treated cells were evaluated at least in duplicate. For each sample, no fewer than 7–8 fields at lower magnification were observed. **d**, Metabolic characteristics of MEKi-treated $CD8^+$ T cells showing OCR, SRC and basal ECAR levels. Representative results from one of the two experiments performed in triplicate are shown. The error bars indicate the s.e.m. Statistical analysis was performed by unpaired, one-tailed Student's *t*-test (*$P \leq 0.05$; ***$P \leq 0.001$; ****$P \leq 0.0001$). FCCP, carbonyl cyanide-4-(trifluoromethoxy)phenylhydrazone. **e**–**i**, Measurement of glucose uptake rates by NBDG incorporation (**e**), *Slc2a1* mRNA expression relative to *Actb* (**f**), proliferation (measured by dilution of Violet CellTrace (VCT)) of pMel-1 $CD8^+$ T cells activated with gp100 peptide in the absence or presence of MEKi and 2DG (**g**), determination of FAO in variously activated pMel-1 $CD8^+$ T cells by expression levels of *Cpt1a* relative to *Actb* (**h**) and incorporation of BODIPY (**i**). Representative results from one of the two experiments performed in triplicate. The error

bars indicate the s.e.m. Statistical analysis was performed by unpaired, one-tailed Student's *t*-test (** $P \leq 0.01$; *** $P \leq 0.001$; **** $P \leq 0.0001$; NS, not significant). **j**,**k**, Estimation of FAO-mediated OCR using palmitate (Palm) as the substrate in the presence or absence of etomoxir (Etx) (**j**); FACS micrograph and statistical analysis of inhibition of proliferation (by VCT dilution) after etomoxir treatment of $CD8^+$ T cells during activation with or without MEKi (**k**). Both **j** and **k** are representative graphs from one of two experiments and shown as mean ± s.e.m. Statistical analysis was performed by unpaired, one-tailed Student's *t*-test (** $P \leq 0.01$; *** $P \leq 0.001$; **** $P \leq 0.0001$). **l**, Number of $CD8^+$ T cells positive for BODIPY, NBDG and PGC1α and respective expression levels (MFI, mean fluorescence intensity) in MEKi-treated TC-1 tumor-bearing vaccinated animals. Representative data from one of two experiments are shown. Each symbol corresponds to one mouse with the indicated number of mice per group given in parentheses. The error bars indicate the s.e.m. Statistical analysis was performed by unpaired, one-tailed Student's *t*-test (* $P \leq 0.05$; ** $P \leq 0.01$). See also Extended Data Fig. 1b.

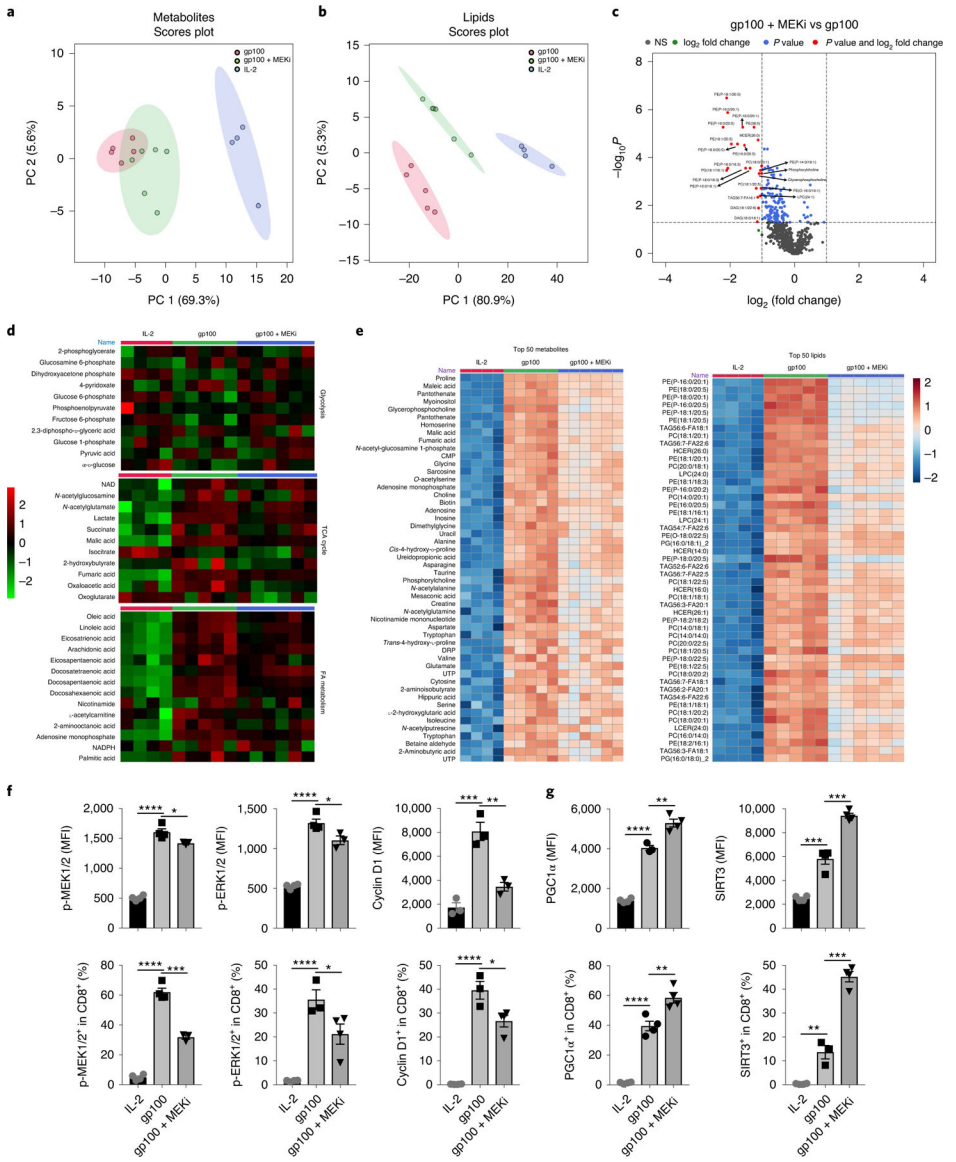

Fig. 3 |. Metabolomic and lipidomic analysis of MEKi-treated CD8+ T cells. a–c, PCA for variously treated cells for different metabolites (**a**) and lipids (**b**), and volcano plot (**c**) to compare metabolites and lipids between gp100 versus gp100 plus MEKi-treated CD8$^+$ T cells. **d**, Heat map analysis of various metabolites in the glycolytic, TCA and FA metabolism cycles. **e**, Heat map analysis showing the top 50 differentially regulated metabolites and lipids between variously treated cells as shown. **f**, Expression (MFI; upper panel) of phosphorylated-(p)-MEK1/2, p-ERK1/2 and cyclin D1 and percentages of cells positive for these molecules (lower panel) after activation of pMel-1 CD8$^+$ T cells with or without MEKi treatment. **g**, Expression of PGC1α and SIRT3 (upper panel) and percentages of cells positive for these molecules (lower panel) after activation of pMel-1 CD8$^+$ T cells with or without MEKi treatment. Both **f** and **g** represent data from one of two experiments shown as mean ± s.e.m. Statistical analysis was performed by unpaired, one-tailed Student's *t*-test (*$P \leq 0.05$; **$P \leq 0.01$; ***$P \leq 0.001$; ****$P \leq 0.0001$).

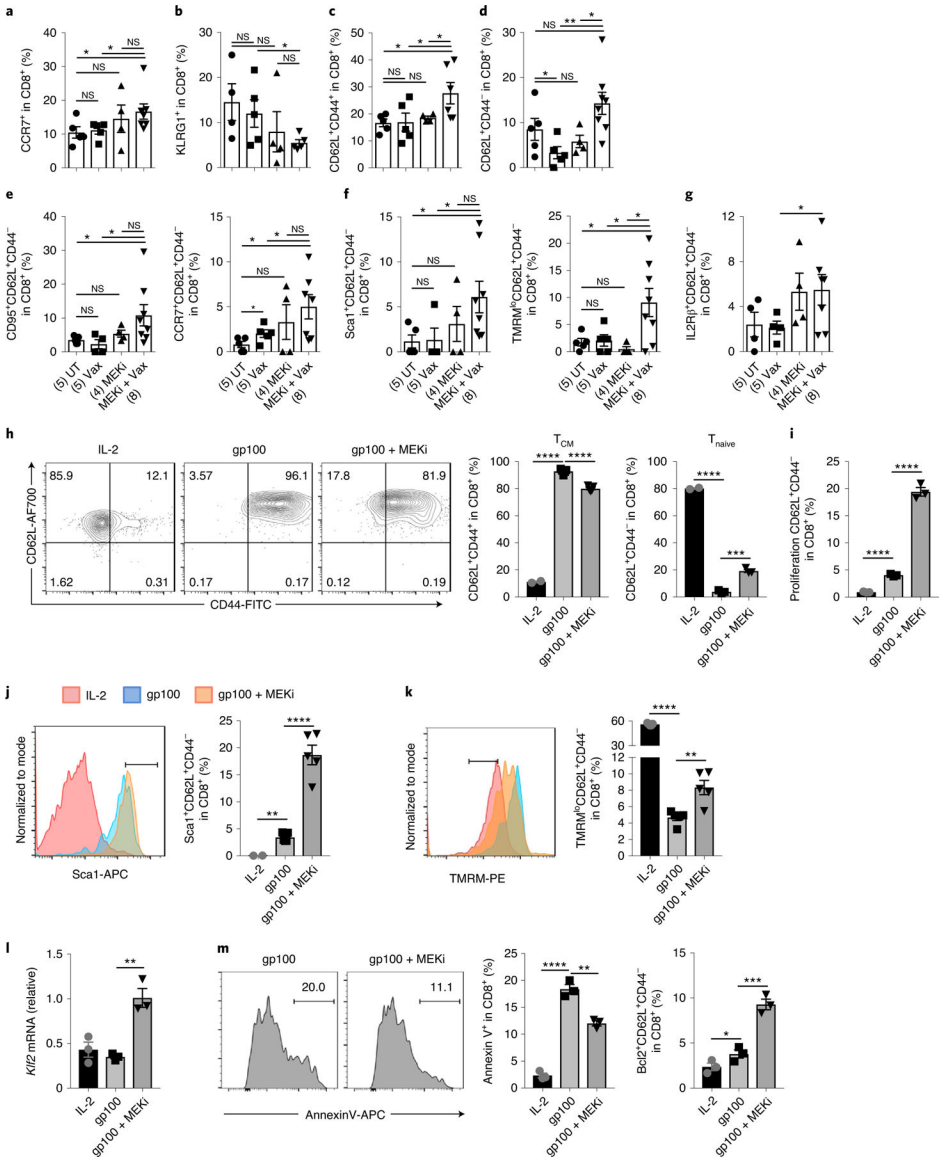

Fig. 4 |. MEKi induces stem cell memory characteristics in CD8+ T cells. a–d, Flow cytometry analysis of $CD8^+$ T cell phenotype in the TME showing frequency of $CCR7^+$ (**a**), $KLRG1^+$ (**b**), T_{CM} ($CD62L^+CD44^+$) (**c**), and T_{naive} ($CD62L^+CD44^-$) (**d**) $CD8^+$ T cells. **e–g**, Frequency of $CD95^+$ and $CCR7^+$ (**e**), $Sca1^+$ and $TMRM^{lo}$ (**f**), and IL-2Rβ^+ cells (**g**) within the T_{naive} ($CD62L^+CD44^-$) population in the TME. Representative data from one of two experiments are shown. Each symbol corresponds to one mouse with the indicated number of mice per group given in parentheses. The error bars indicate the s.e.m. Statistical analysis was performed by unpaired, one-tailed Student's *t*-test (*$P \leq 0.05$; **$P \leq 0.01$; NS, not significant). **h**,**i**, FACS analysis of variously in vitro–activated pMel-1 $CD8^+$ T cells for memory characteristics (T_{CM} ($CD62L^+CD44^+$) and T_{naive} ($CD62L^+CD44^-$)) (**h**) and proliferation (by VCT dilution) in $CD62L^+CD44^-$ cells (**i**). Representative data from one of the three experiments performed in triplicate are shown as mean ± s.e.m. Statistical analysis was performed by unpaired, one-tailed Student's *t*-test (***$P \leq 0.001$; ****$P \leq$

0.0001). **j**,**k**, Expression of Sca1 on naive T cells ($CD62L^+CD44^-$) (**j**) and mitochondrial potential of $CD62L^+CD44^-CD8^+$ T cells estimated by incorporation of TMRM dye (**k**) after respective activation as in **h**. A representative graph from one of three experiments is shown as mean ± s.e.m. Statistical analysis was performed by unpaired, one-tailed Student's *t*-test (** $P \leq 0.01$; **** $P \leq 0.0001$). **l**,**m**, mRNA expression levels of *Klf2* relative to *Actb* (**l**) and percentages of annexin V^+ and $Bcl2^+CD62L^+CD44^-$ in $CD8^+$ T cells (**m**) in variously activated $CD8^+$ T cells. Experiments were repeated at least three times in triplicate and are represented as mean ± s.e.m. Statistical analysis was performed by unpaired, one-tailed Student's *t*-test (* $P \leq 0.05$; ** $P \leq 0.01$; *** $P \leq 0.001$; **** $P \leq 0.0001$). See also Extended Data Figs. 2 and 3.

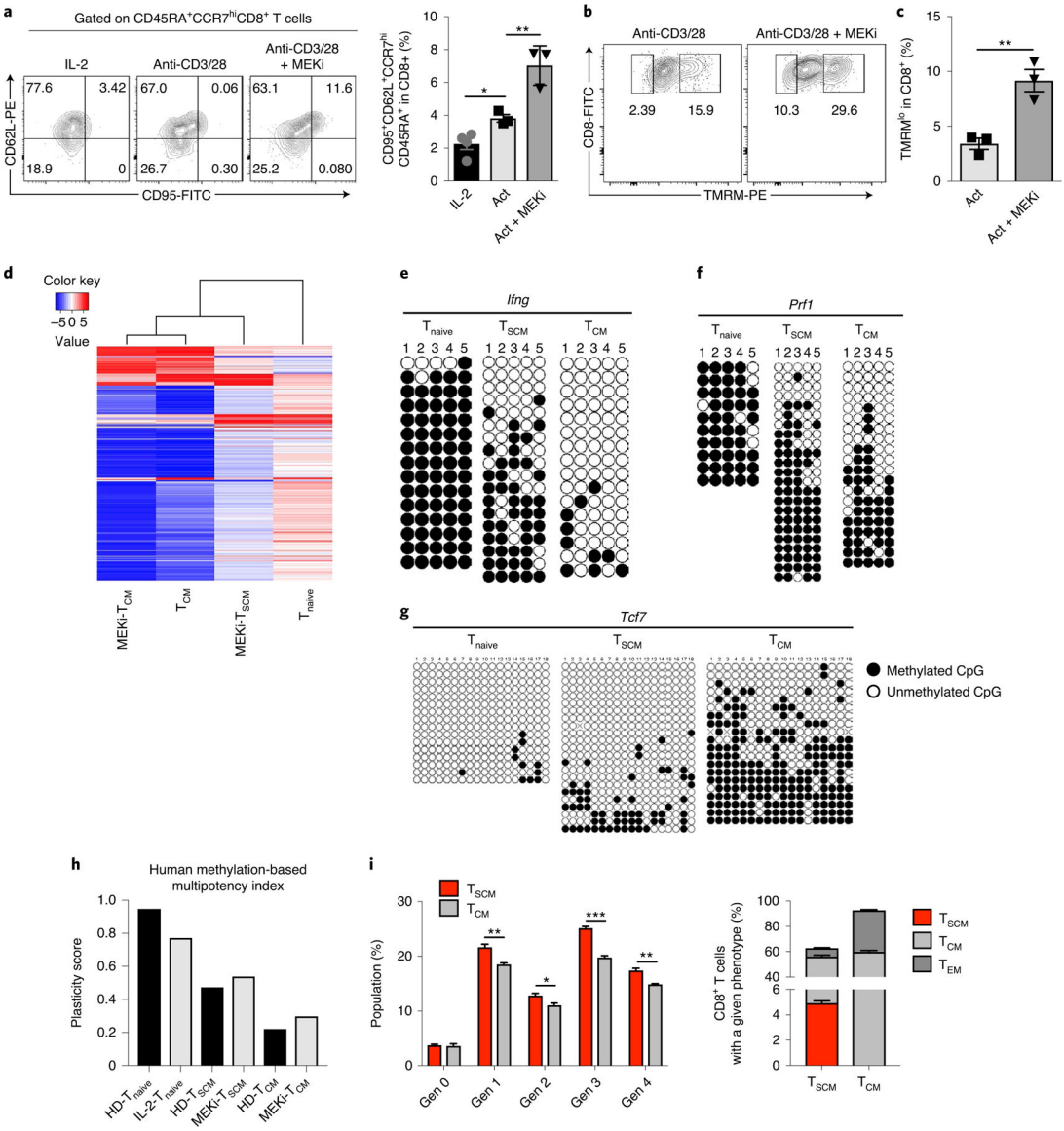

Fig. 5 |. MEKi induces stem cell memory in human CD8+ T cells that is intermediate between that of Tnaive and TCM cells. a–c,

FACS graphs and statistical analysis of induction of $CD45RA^+CCR7^{hi}CD62L^+CD95^+$ (**a**) and $TMRM^{lo}$ (**b**,**c**) $CD8^+$ T cells after 72 h of activation as described in the Methods. Representative FACS graphs from one of three experiments are shown as mean ± s.e.m. Statistical analysis was performed by unpaired, one-tailed Student's *t*-test (*$P \leq 0.05$; **$P \leq 0.01$). See also Extended Data Fig. 4a. **d**–**g**, Whole-genome and loci-specific bisulfite sequencing analysis of variously activated human $CD8^+$ T cells. **d**, Heat map showing the top 3,000 CpGs in variously treated cell types selected in an unbiased manner (see also Extended Data Fig. 4b). Methylation status of *Ifng* (**e**), *Prf1* (**f**) and *Tcf7* (**g**) gene loci in naive, T_{SCM} and T_{CM} $CD8^+$ T cells. Horizontal lines represent individual sequenced clones from the pool of FACS-purified $CD8^+$ T cells. **h**, Plasticity score derived from the methylation-based multipotency index of variously treated human $CD8^+$ T cells (compared with healthy donor (HD) cells). Representative data from one of two experiments performed

at different time points are shown. See also Extended Data Fig. 4c for average methylation and statistical analysis. **i**, Estimation of proliferation capacity and multipotency of T_{SCM} and T_{CM} cells. For proliferation estimation, sorted T_{SCM} and T_{CM} cells generated from pMel-1 $CD8^+$ cells after gp100 plus MEKi treatment were further activated with gp100 for another 24 h followed by determination of the percentage of cells in various generations of cell division estimated by VCT dilution. For determination of multipotency of T_{SCM} and T_{CM} cells, the two cell populations were reactivated with gp100 followed by estimation of the generation of T_{SCM} and T_{CM} and T_{EM} cells. Representative results from one of two experiments are shown. The error bars indicate the s.e.m. Statistical analysis was performed by unpaired, one-tailed Student's *t*-test (*$P \leq 0.05$; **$P \leq 0.01$; ***$P \leq 0.001$).

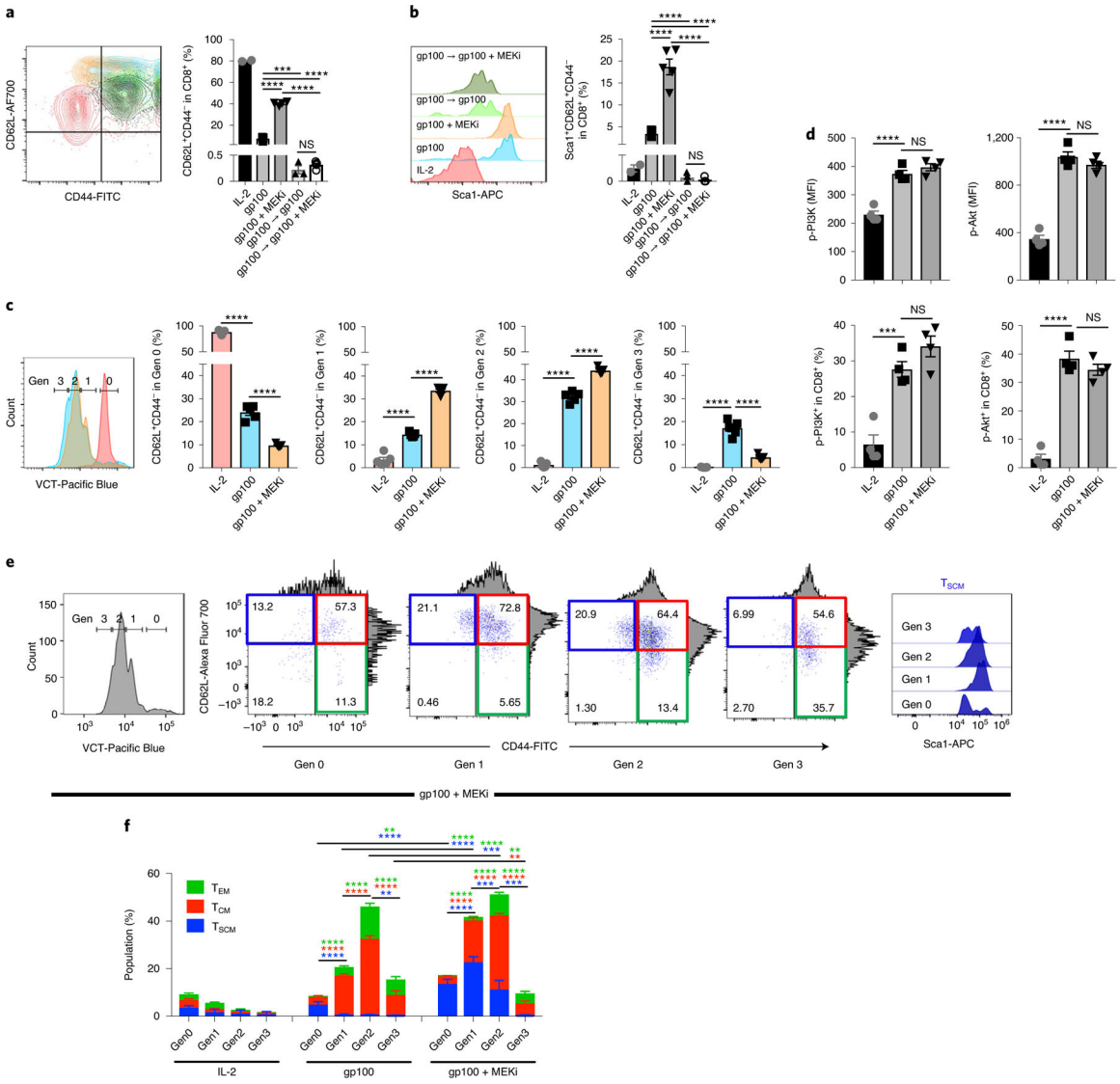

Fig. 6 |. MEKi induces TSCM cells by delaying cell division, proliferation and differentiation. a,b,

pMel-1 CD8$^+$ T cells were activated with gp100 or gp100 plus MEKi for 48 h followed by FACS analysis (first time point). Cells activated with gp100 were reactivated with either gp100 or gp100 plus MEKi for an additional 48 h followed by FACS analysis (second time point). Cells treated with IL-2 were used as a control. Representative flow micrographs and statistical analysis of the frequency of CD62L$^+$CD44$^-$ cells in pMel-1 CD8$^+$ T cells (**a**) and frequency of Sca1$^+$ cells in CD62L$^+$CD44$^-$ population in pMel-1 CD8$^+$ T cells (**b**). Data are representative of three experiments performed in triplicate. The error bars indicate the s.e.m. Statistical analysis was performed by unpaired, one-tailed Student's *t*-test (***$P \leq 0.001$; ****$P \leq 0.0001$; NS, not significant). **c**, The proliferation profile of pMel-1 CD8$^+$ T cells after activation with gp100 peptide in the presence or absence of MEKi for 48 h. Frequency of naive cells (CD62L$^+$CD44$^-$) in different generations (Gen) of cell division is shown in the bar graphs. **d**, Determination of expression (MFI; upper panel) and the numbers (lower panel) of pMel-1 CD8$^+$ T cells having phosphorylated(p)-PI3K and Akt after activation

with or without MEKi treatment. A representative graph from one of two experiments is shown for **c** and **d**. The error bars indicate the s.e.m. Statistical analysis was performed by unpaired, one-tailed Student's *t*-test (***$P \leq 0.001$; ****$P \leq 0.0001$; NS, not significant). See also Extended Data Fig. 2d. **e**, Flow micrographs showing different types of memory cells in various generations of cell division (Gen0–Gen3) on the basis of the expression of CD62L and CD44 after gp100 plus MEKi treatment. T_{SCM} cells were analyzed on the basis of the expression of Sca1 on cells in the naive compartment ($CD62L^{+}CD44^{-}$) (rightmost panel). **f**, Statistical analysis of the cell types (T_{SCM}, T_{CM} and T_{EM}) present in various generations obtained after activation of pMel-1 $CD8^{+}$ T cells with gp100 peptide in the presence or absence of MEKi for 48 h. Experiments were repeated twice with similar results and representative results from one experiment are shown. The error bars indicate the s.e.m. Statistical analysis was performed by unpaired, one-tailed Student's *t*-test, with the asterisks colored to indicate the comparison: blue, comparison to T_{SCM}; red, comparison to T_{CM}; green, comparison to T_{EM} (**$P \leq 0.01$; ***$P \leq 0.001$; ****$P \leq 0.0001$).

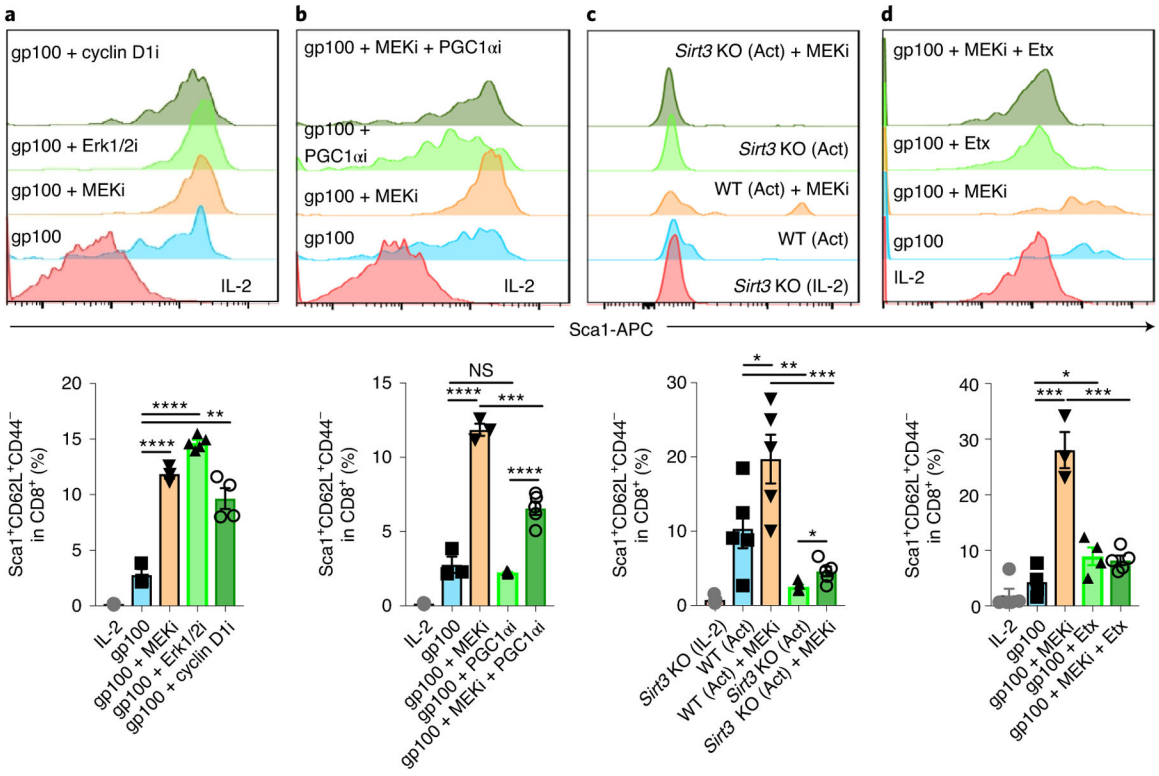

Fig. 7 |. MEKi induces FAO-mediated stem cell memory in T cells. a,b, Representative flow micrographs and statistical analysis of the frequency of $Sca1^+$ cells in the $CD62L^+CD44^-$ population in pMel-1 $CD8^+$ T cells after 48 h of activation in the presence of ERK1/2 and cyclin D1 inhibitors (**a**) and PGC1αi with and without MEKi (**b**). Data are representative of two experiments performed in triplicate. The error bars indicate the s.e.m. Statistical analysis was performed by unpaired, one-tailed Student's *t*-test (**$P \leq 0.01$; ***$P \leq 0.001$; ****$P \leq 0.0001$; NS, not significant). **c**, Wild-type (WT) and *Sirt3* knockout (KO) cells were activated for 72 h with anti-CD3 and anti-CD28 with or without MEKi followed by estimation of the frequency of $Sca1^+$ cells in the $CD62L^+CD44^-$ population. Data are representative of two experiments performed in triplicate. The error bars indicate the s.e.m. Statistical analysis was performed by unpaired, one-tailed Student's *t*-test (*$P \leq 0.05$; **$P \leq 0.01$; ***$P \leq 0.001$). **d**, Representative flow micrographs and statistical analysis of the frequency of $Sca1^+$ cells in $CD62L^+CD44^-$ population in pMel-1 $CD8^+$ T cells after 48 h of activation in the presence of etomoxir (Etx) with and without MEKi. Data are representative of two experiments performed in triplicate. The error bars indicate the s.e.m. Statistical analysis was performed by unpaired, one-tailed Student's *t*-test (*$P \leq 0.05$; ***$P \leq 0.001$). See also Extended Data Fig. 4d.

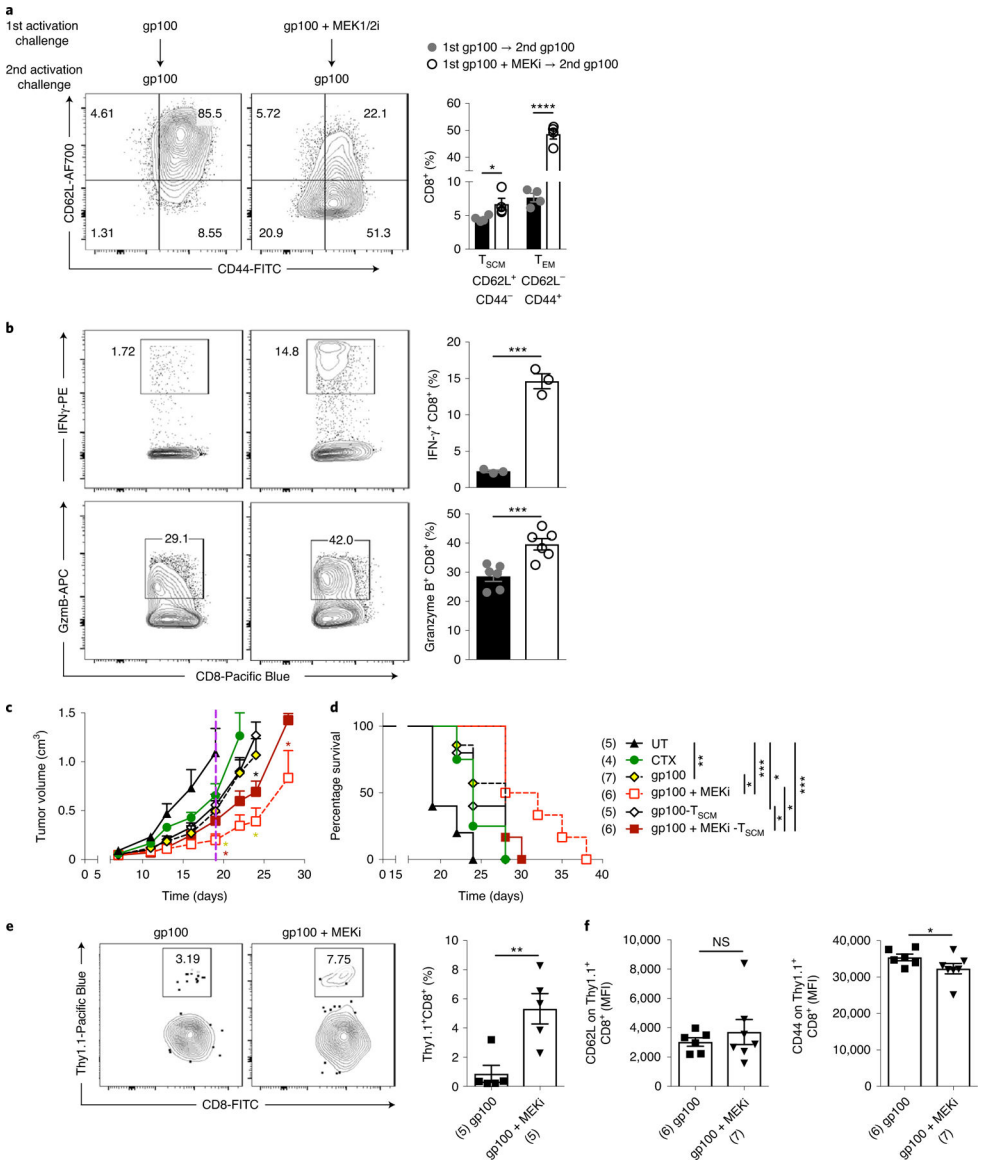

Fig. 8 |. MEKi-treated CD8+ T cells have higher recall responses leading to stronger TSCM-mediated antitumor effects after ACT. a,b,

FACS analysis of phenotype (T_{SCM} and T_{EM}) of activated pMel-1 $CD8^+$ T cells (gp100 versus gp100 + MEKi) after antigen rechallenge with gp100 peptide for 48 h (**a**). Estimation of the expression of effector molecules (IFN-γ and granzyme B) in respectively rechallenged groups (**b**). Representative results from one of three experiments performed in triplicate are shown. The error bars indicate the s.e.m. Statistical analysis was performed by unpaired, one-tailed Student's *t*-test (*$P \leq 0.05$; ***$P \leq 0.001$; ****$P \leq 0.0001$). **c**,**d**, ACT of B16F10 tumor-bearing mice with activated pMel-1 $CD8^+$ T cells (with or without MEKi). One day before cell transfer mice were treated with a low dose of cytoxan (CTX, 100 mg kg^{-1}). Total pMel-1 $CD8^+$ T cells were activated with gp100 with or without MEKi and 1×10^6 cells were transferred into tumor-bearing mice. In one treatment group, $CD62L^+CD44^-Sca1^+$ T_{SCM} cells were depleted after gp100 ± MEKi treatment and 1×10^6 T_{SCM}-depleted $CD8^+$ T cells were transferred into B16F10 tumor-bearing mice. Tumor

growth profile (**c**) and mouse survival after various treatments (**d**) as indicated in the figure are shown. A representative of two experiments is shown. Each symbol corresponds to one mouse with the indicated number of mice per group given in parentheses. The error bars indicate the s.e.m. Statistical analysis was performed by unpaired, one-tailed Student's *t*-test, with the asterisks colored to indicate the comparison: yellow, comparison between gp100 and gp100 + MEKi; dark red, comparison between gp100 + MEKi and gp100 + MEKi-T_{SCM}; and black, comparison between gp100-T_{SCM} and gp100 + MEKi-T_{SCM} in tumor growth graph in **c** (*$P \leq 0.05$; **$P \leq 0.01$; ***$P \leq 0.001$). See also Extended Data Fig. 5a for cell engraftment and Extended Data Fig. 5b. **e**,**f**, Estimation of numbers of adoptively transferred Thy1.1 $CD8^+$ T cells in tumors of variously treated mice 30 days after ACT. For the gp100-treated group whereby the endpoint for euthanasia was reached earlier, the mice were killed and tumors were collected and stored as single-cell suspensions at −80 °C. At the end of the study, all samples were processed and stained together for FACS analysis to check the percentages of adoptively transferred cells (Thy1.1) (**e**) and the expression of CD62L and CD44 on these cells (**f**). A representative of two experiments is shown. Each symbol corresponds to one mouse with the indicated number of mice per group given in parentheses. The error bars indicate the s.e.m. Statistical analysis was performed by unpaired, one-tailed Student's *t*-test (*$P \leq 0.05$; **$P \leq 0.01$; NS, not significant). See also Extended Data Fig. 5c–e.